공학박사학위논문

공기층을 포함한 이상적인 초소수성 표면을 가진 난류채널유동의 직접수치해석

Direct numerical simulation of turbulent channel flow with an idealized superhydrophobic surface having an air layer

2016 년 2 월

서울대학교 대학원

기계항공공학부

정 태 용

Direct numerical simulation of turbulent channel flow with an idealized superhydrophobic surface having an air layer

Taeyong Jung

Department of Mechanical & Aerospace Engineering
Seoul National University

Abstract

The slip effect on a superhydrophobic surface in a turbulent boundary layer determines the performance of a skin-friction drag reduction, and it is affected by the superhydrophobic grating parameters. With the assumption that the air-water interface is flat, direct numerical simulations of turbulent channel flow with superhydrophobic surfaces having an air layer are conducted in the present study. First, an idealized superhydrophobic surface (i.e., without any supporting structures inside the air layer) is considered as a slippery surface for keeping only its useful effects (Busse *et al.*, 2013; Jung, Choi & Kim, 2016). Inside the air layer, both the shear-driven flow and recirculating flow with zero net mass flow rate are considered. With increasing air-layer thickness, the slip length, slip velocity and percentage of drag reduction increase. At a given air-layer thickness, the shear-driven flow in the air layer supplies more slip than the recirculating flow. It is shown that the slip length is independent of the water-flow condition and depends only on the air-layer geometry. The amount of drag reduction obtained is in between those by the empirical formulae from

the streamwise slip only and isotropic slip, indicating that the present air-water interface generates an anisotropic slip, and the streamwise slip length (b_x) is larger than the spanwise one (b_z). From the joint probability density function of the slip velocities and velocity gradients at the interface, we confirm the anisotropy of the slip lengths and obtain their relative magnitude ($b_x/b_z = 4$) for the present idealized superhydrophobic surface. It is also shown that the Navier slip model is valid only in the mean sense, and it is generally not applicable to fluctuating quantities. Second, the superhydrophobic surface with longitudinal grooves is considered. The surface grating parameters are the air-layer thickness, pitch length and gas fraction. A wide range of pitch lengths are simulated from microscale $O(1)$ to macroscale $O(10^2)$ in the viscous wall unit. The minimal channel flow (Jiménez & Moin, 1991) is adopted for a microgrooved surface. Since the small pitch length is accompanied by small groove width, the growth of the slip velocity at the air-water interface is inhibited. At a large pitch length, however, the percentage of drag reduction obtained is saturated with the gas fraction as the air-layer thickness increases. For SHSs with grooves, the slip lengths for the instantaneous velocity components (b_x and b_z) varies at the air-water interface in the spanwise direction.

Keywords: turbulent flow, skin-friction drag, air-water interface,
superhydrophobic surface, anisotropic slip

Student number: 2009-31250

Contents

List of Figures

Figure

List of Tables

Table

Chapter 1

Introduction

1.1 Motivation

A skin-friction reduction is an important issue undoubtedly in the engineering fields because the drag on the moving object, such as an aircraft, car, ship, submarine, has a detrimental effect on the fuel efficiency. Therefore, there are numerous approaches have been developed in order to reduce the skin-friction drag, especially in turbulent boundary layers. Examples of successful strategies for skin-friction reduction include both active and passive approaches, such as opposite blowing and suction (Choi, Moin & Kim, 1994), riblets (Choi, Moin & Kim, 1993), permeable walls (Hahn, Je & Choi, 2002), polymer additives (Min *et al.*, 2003), compliant walls (Kang & Choi, 2000; Kim & Choi, 2015), transverse cavities (Hahn, 2002).

The skin-friction drag occurs when an object moves in a viscous fluid and it is proportional to a viscosity of fluid. The viscosity of water is much larger than that of air (almost 50 times under the standard condition), so waterborne crafts (e.g., ship, submarine, torpedo, etc.) can experience more viscous drag than airborne crafts or ground vehicles. Therefore, many studies for the skin-friction drag reduction in water have been conducted and the one of successful strategies is a lubrication using air. Two review papers published in 2010 with respect to the lubrication: air layer lubrication (Ceccio, 2010) and superhydrophobic

surface (SHS) (Rothstein, 2010). These techniques segregate the water flow from contact with the no-slip wall. The former can generate the very large drag reduction ($\sim$ 100%) but needs the additional cost (Elbing *et al.*, 2008), whereas the latter can produce a significant drag reduction ($\sim$ 75%) without any additional cost (Park, Sun & Kim, 2014). The most important aspect of the lubrication is the violation of the classical no-slip boundary condition.

1.2 Backgrounds

The surface property whether slippery or not is determined by the molecular dynamics of solid and intermolecular forces. Young showed the relation between the surface tension and contact angle, θ, which the air-water interface intersects with the solid surface (Goldstein & Council, 1965).

$$\cos\theta = \frac{\sigma_{sg} - \sigma_{sl}}{\sigma_{lg}}. \tag{1.1}$$

where σ_{sg} is the solid-gas surface tension, σ_{sl} is the solid-liquid surface tension, and σ_{lg} is the liquid-gas surface tension. Either wetting or non-wetting state is represented by the contact angle, and the contact angle less than 90° usually indicates that wetting of the surface is favorable. The contact angles greater than 90° generally means that wetting of the surface is unfavorable, so the fluid will minimize contact with the surface and form a compact liquid droplet. For water, a wettable surface may also be termed *hydrophilic* and a nonwettable surface is termed *hydrophobic*. In practice, the contact angle is below 150° for a hydrophobic surface.

Superhydrophobic surfaces (SHSs) are highly hydrophobic (i.e. extremely difficult to wet) surfaces which have the contact angle greater than 150, showing almost no contact between the liquid drop and the surface. The SHS was initially inspired the significant water repellance of the lotus leaf, so the superhydrophobicity is also called the lotus effect. Since the lotus leaf has many random micro/nano structures on its surface, the air layer can be entrapped inside the surface roughnesses. This is because that SHSs have a surface texture such as ridges or posts. With this condition (as known as the Cassie-Baxter state; see figure 1.1(a)), the slip occurs at the interface between water and air

and this slip effect is known as the drag reduction (DR) mechanism of SHS.

The slip refers to the situation where the value of tangential velocity component is different from that of the solid surface in contact with it (Lauga, Brenner & Stone, 2007). Navier (1823) suggested the slip boundary condition as

$$u_s = b_x \left(\frac{\partial u}{\partial y}\right)_s, \quad w_s = b_z \left(\frac{\partial w}{\partial y}\right)_s, \tag{1.2}$$

where u_s and w_s are the slip velocities in the streamwise and spanwise directions, and $(\partial u/\partial y)_s$ and $(\partial w/\partial y)_s$ are the velocity gradients in the streamwise and spanwise directions at the slippery surface. In this thesis, (x, y, z) are the streamwise, wall-normal, and spanwise directions, respectively, (u, v, w) are the corresponding velocity components, and the subscript 's' denotes the value at the slippery surface. From the relationship between the slip velocity and velocity gradient at the surface, b_x and b_z which are the most important variables in this thesis are obtained. They are called the streamwise and spanwise *slip lengths*. The magnitude of slip is quantified by the slip length and it is represented as the fictitious distance below the slippery surface where the no-slip condition would be satisfied (see figure 1.2). In general, there are two separate slip lengths for the mean velocity components: one is the apparent slip length (b_{app}, or Navier slip length) which is defined at the non-textured surface (figure 1.2(a)) and the other is the effective slip length (b_{eff}) which is defined at the textured surface (figure 1.2(b)).

For maintaining the Cassie-Baxter state, the air-water interface has to sustain against the pressure difference between water and air. The sustainable condition for the interface over longitudinal grooves are expressed by Young-

Laplace equation as

$$\Delta p_{max} = p_{water} - p_{air} = \frac{2\sigma \cos(\pi - \theta)}{L_g}, \tag{1.3}$$

where p is the pressure, θ is the contact angle, and L_g is the groove width. As L_g increase, the endurable pressure difference (Δp_{max}) decreases and thus there is a size limitation of the groove width.

The effective slip length of SHS is on the order of 200-400 μm have been reported (Lee, Choi & Kim, 2008; Lee & Kim, 2009). Thus, SHSs can be applied for the self-cleaning, anti-biofouling, anti-icing, and skin-friction reduction of water flow. In the next section, the flow control using SHS as a passive device will be discussed.

1.3 Literature reviews

To avoid the complexity of simulating two-phase flow, most theoretical and numerical studies related to superhydrophobic surface (SHS) have not considered the air layer over SHSs but modeled it by using either the Navier slip model or the effective slip model. The Navier slip model that provides slip velocities in the wall-parallel directions at the air-water interface have been widely used for a numerical simulation of turbulent flows due to its easy implementation. The slip velocities for boundary conditions is determined by equation 1.2 with the prescribed slip lengths, so this model is proper to describe the hydrophobic surface or chemically slippery surface. Fukagata, Kasagi & Koumoutsakos (2006) argued that the Navier slip model using the prescribed effective slip-length (b_{eff}) can be an approximate SHS model for the boundary condition. For a laminar channel flow, the analytical solution can be readily obtained (Rothstein, 2010). However, the main weakness of this slip model is that the slip lengths b_x and b_z are unknown, and thus they have to be prescribed *a priori*. Note that the slip length is dependent on the flow condition. To overcome this limitation, the pattern of SHS have been reflected by using mixed boundary conditions consisting of no-slip (solid-water interface) and no-shear (air-water interface) regions. In addition to the assumption of a shear-free condition at the interface between water and air, the air-water interface is assumed to be flat and thus the surface tension effect is neglected. It is called the effective slip model and this model was initially suggested by Philip (1972a). Philip (1972a) and Philip (1972b) derived analytical solutions for Stokes flow over a flat plate with longitudinal or transverse free-slip regions (Jelly, Jung & Zaki, 2014). From the analytical solutions of Philip (1972a) and Philip (1972b), Lauga & Stone (2003) suggested that the effective slip length of SHS with longitudinal grooves for laminar flow

is a function of gas fraction and the pitch length (pattern size) as

$$b_{eff} = \frac{L_p}{\pi} \ln \left[\sec \left(\frac{\pi \phi}{2} \right) \right], \tag{1.4}$$

where L_p is the pitch length and ϕ is the gas fraction. The pitch length is defined as the summation of the width of one groove and ridge, and the gas fraction is defined as the groove width divided by the pitch length. The effective slip length of SHS with transverse grooves is a half of that with longitudinal grooves (Lauga & Stone, 2003). Equation 1.4 have been validated by experimental and numerical studies (Lee, Choi & Kim, 2008; Teo & Khoo, 2009; Park, Park & Kim, 2013). For turbulent flows, however, the assumption of a shear-free interface has not been validated.

In a laminar channel flow, the drag reduction (DR) rate and the slip velocity are a function of the slip length and they can be easily derived (Choi *et al.*, 2006; Rothstein, 2010) as

$$DR = \frac{6b}{6b + H}, \tag{1.5}$$

where DR is the DR rate, b is the slip length, and H is the channel height. On the other hand, the DR rate in turbulent flow is unpredictable and thus experimental studies have been conducted to investigate DR in turbulent flows (Watanabe, Yanuar & Udagawa, 1999; Zhao, Du & Shi, 2007; Daniello, Waterhouse & Rothstein, 2009; Peguero & Breuer, 2009; Woolford *et al.*, 2009; Jung & Bhushan, 2010; Aljallis *et al.*, 2013; Park, Sun & Kim, 2014). While Daniello, Waterhouse & Rothstein (2009) and Park, Sun & Kim (2014) experimentally showed significant turbulent DRs (50% and 75%, respectively) with SHSs, others reported negligible DR or even drag increase in a turbulent flow (Watanabe, Yanuar & Udagawa, 1999; Zhao, Du & Shi, 2007; Peguero & Breuer, 2009; Al-

jallis *et al.*, 2013). This inconsistency may be explained by the air loss inside cavities (as known as Wenzel state, figure 1.1(b))), deformation of an air-water interface, errors in measuring friction drag, etc. (Park, Sun & Kim, 2014).

To understand the flow changes and mechanism of DR by SHSs, many numerical studies have been conducted (Min & Kim, 2004; Fukagata, Kasagi & Koumoutsakos, 2006; Martell, Perot & Rothstein, 2009; Busse & Sandham, 2012; Park, Park & Kim, 2013; Jelly, Jung & Zaki, 2014; Türk *et al.*, 2014; Rastegari & Akhavan, 2015; Seo *et al.*, 2015). These numerical studies have reported DR in turbulent flow, and provided the mechanism by which DR was achieved. Min & Kim (2004) showed that the turbulent drag is reduced by streamwise slip but increased by spanwise slip. Fukagata, Kasagi & Koumoutsakos (2006) proposed an empirical formula for the DR rate. Busse & Sandham (2012) investigated the effects of the anisotropic slip (i.e., different slip in wall-parallel directions) as well. These studies did not consider the SHS geometry but prescribed a constant slip length at the slippery surface. Martell, Perot & Rothstein (2009) simulated the flows over longitudinal grooves and square posts by using mixed boundary conditions consisting of no-slip (solid-water interface) and no-shear (air-water interface) regions. Park, Park & Kim (2013) found, by considering different SHS geometries and Reynolds numbers, that the amount of turbulent DR is well correlated with the slip length normalized by the viscous wall unit. Jelly, Jung & Zaki (2014) addressed the effect of secondary flow induced by the edges of the longitudinal groove, and Türk *et al.* (2014) found that the groove width significantly changes the flow pattern. More recently, Rastegari & Akhavan (2015) suggested that the amount of DR should be expressed as the sum of the slip velocity and the modifications of the Reynolds shear stress and mean convective stress. Seo *et al.* (2015) investigated the effect of the surface geometry (i.e. longitudinal grooves vs. square posts) on pres-

sure fluctuations at the interface and suggested a relationship between the slip velocity and the root-mean-square (rms) pressure fluctuations at the interface.

According to equation 1.4, the larger DR rate can be achieved with the larger groove width ($L_g = L_p\phi$), but the larger groove width has an influence on the stability of the air-water interface (equation 1.3). Very recently, Türk *et al.* (2014) and Seo *et al.* (2015) examined the sustainability of the interface between water and air against turbulent pressure fluctuations. They showed that the maintenance of the air-water interface depends on the pitch length of SHSs, and reported that the maximum sizes of the longitudinal grooves and square posts for its maintenance are about 150 and 50 wall units, respectively. Seo *et al.* (2015) also showed that the interface deformation by turbulent pressure fluctuations is negligible when the pitch length of SHS is equal to 6 wall units with the capillary number of $Ca = 6 \times 10^{-3}$, where $Ca = \mu_l u_\tau/\sigma$, μ_l is the water viscosity, u_τ is the shear velocity, and σ is the surface tension between air and water ($\sigma = 0.073$ N/m). Also, the capillary number is very small for many microfluidic applications in laminar flows, and thus the curvature effects of the air-water interface can be neglected (Cottin-Bizonne *et al.*, 2004; Ybert *et al.*, 2007; Teo & Khoo, 2009). Piao & Park (2015) modeled pressure fluctuations at the interface as a harmonic oscillation and suggested that the smaller pitch length should be required for the air-water interface to be stable.

Despite many achievements through previous numerical studies, most of them have not considered the air layer inside the cavity or groove but modeled it by prescribing either a slip velocity (Min & Kim, 2004; Fukagata, Kasagi & Koumoutsakos, 2006; Busse & Sandham, 2012) or a shear-free condition (Martell, Perot & Rothstein, 2009; Park, Park & Kim, 2013; Jelly, Jung & Zaki, 2014; Türk *et al.*, 2014; Rastegari & Akhavan, 2015) at the interface. Only a few studies have considered the air layer for laminar flow (Tretheway

& Meinhart, 2004; Davies *et al.*, 2006; Maynes *et al.*, 2007; Busse *et al.*, 2013) assuming flat air-water interface.

There are various features of SHS, and the representative supporting structures of SHS are ridges (or grooves) and posts. Cheng, Teo & Khoo (2009) considered four different features to investigate the effect of the shape of SHS on the effective slip length: longitudinal grooves, transverse grooves, square holes and square posts. They showed that the longitudinal grooves have the largest effective slip length where the gas fraction (ϕ) is up to 90%. The effective slip length of square posts is larger than that of longitudinal grooves at $\phi > 0.9$. However, the effective slip length decreases as the Reynolds number increases with three different shapes except the longitudinal grooves. As a result, when the Reynolds number is above 300, the effective slip length of SHS with longitudinal grooves is larger than that with square posts at $\phi > 0.9$. For turbulent flow, Daniello, Waterhouse & Rothstein (2009) and Park, Sun & Kim (2014) experimentally showed significant drag reductions (50% and 75%, respectively) with the longitudinal grooves. Therefore, many previous studies have been conducted by considering the longitudinal grooves as the feature of SHS (Martell, Perot & Rothstein, 2009; Park, Park & Kim, 2013; Jelly, Jung & Zaki, 2014; Türk *et al.*, 2014; Rastegari & Akhavan, 2015).

1.4 Objectives

The objectives of the present study are to investigate the effects of SHS on the slip length and skin-friction drag in turbulent flow. First, the effects of air-flow type inside SHS are investigated in turbulent flow over an idealized SHS. Second, the effects of surface grating parameters are investigated in turbulent flow over SHS having longitudinal grooves/ridges. For these purpose, direct numerical simulations (DNS) are performed in a turbulent channel flow with various scale of SHS.

This thesis is organized as follows. Chapter 2 includes the governing equations, numerical methods, computational details, and the analytical and numerical solutions of fully developed laminar channel flow with SHS. In Chapter 3, the effects of an idealized SHS on the apparent slip length and skin-friction drag are presented. In Chapter 4, the effects of surface grating parameters of SHS on the effective slip length and turbulent drag are presented. Finally, the summary and concluding remarks are followed in Chapter 5.

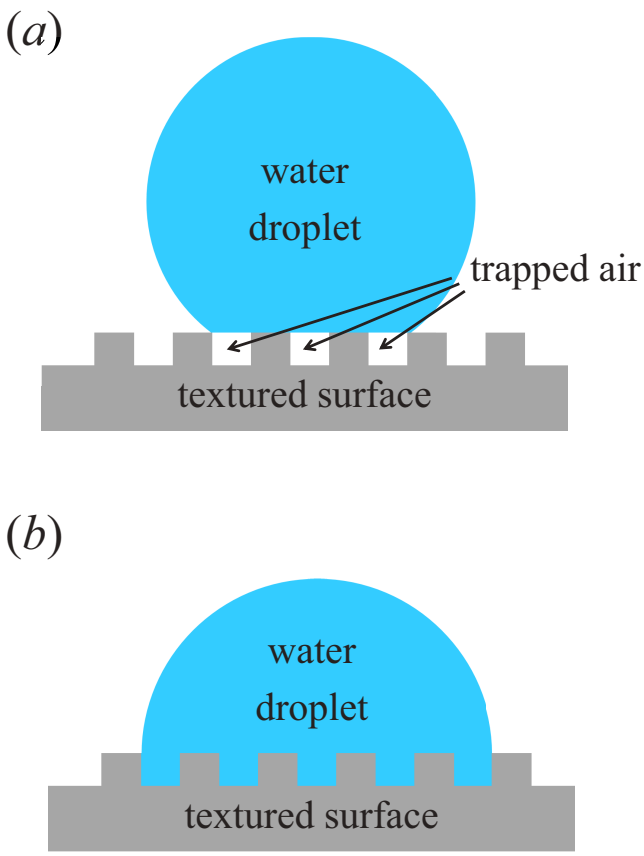

Figure 1.1. Wetting states of textured surface: (a) the Cassie-Baxter state; (b) the Wenzel state.

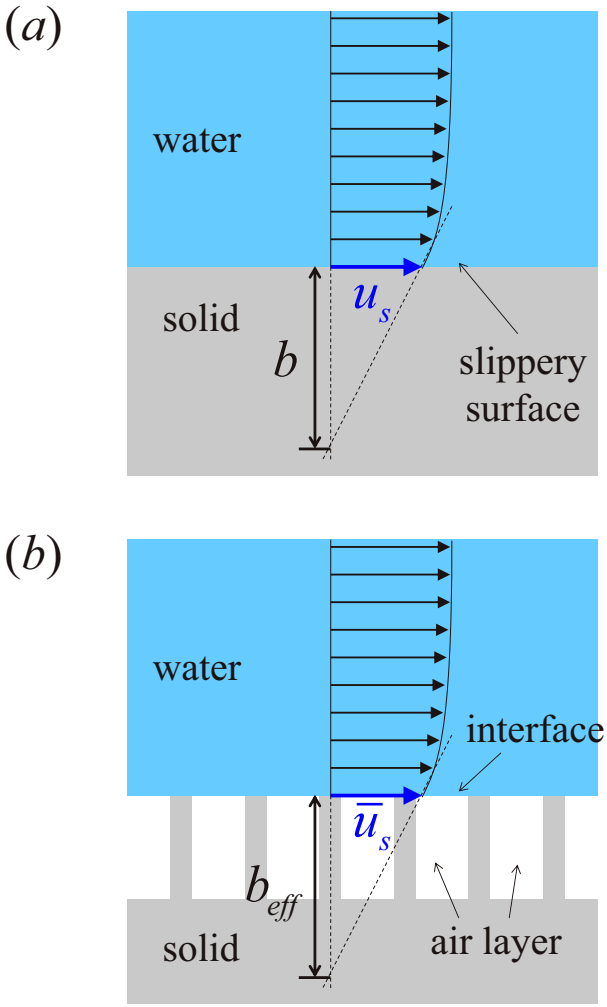

Figure 1.2. Definition of the slip length: (a) at the non-textured surface; (b) at the textured surface.

Chapter 2

Numerical methods

2.1 Governing equations

The governing equations for DNS are the unsteady incompressible Navier–Stokes and continuity equations:

$$\rho_\varphi \left(\frac{\partial u_i}{\partial t} + \frac{\partial}{\partial x_j} u_i u_j \right) = -\frac{\partial p}{\partial x_i} + \mu_\varphi \frac{\partial^2 u_i}{\partial x_j \partial x_j} + \Pi_\varphi \delta_{1i} + f_i, \tag{2.1}$$

$$\frac{\partial u_i}{\partial x_i} - q = 0, \tag{2.2}$$

where t is the time, $(x_1, x_2, x_3) = (x, y, z)$ are the streamwise, wall-normal, and spanwise directions, respectively, $(u_1, u_2, u_3) = (u, v, w)$ are the corresponding velocity components, p is the pressure, ρ_φ and μ_φ are the density and viscosity of water or air, respectively, and Π_φ is the source term for driving the water or air flow. The subscript 'φ' denotes water ($\varphi = l$; liquid) or air ($\varphi = g$; gas). Working fluid properties are $\rho_l = 998$ kg/m^3, $\rho_g = 1.2$ kg/m^3, $\mu_l = 1.0 \times 10^{-3}$ Pa·s, and $\mu_g = 1.8 \times 10^{-5}$ Pa·s (under the standard condition: 20°C and 1 atm). Π_l is the mean pressure gradient necessary to drive the water flow with a fixed mass flow rate, and Π_g is the forcing term to determine the flow type inside the air layer. An immersed boundary method (Kim, Kim & Choi, 2001) is used to satisfy the no-slip boundary condition on the texture geometry of the SHS. f_i

and q, respectively, are the momentum forcing and the mass source/sink defined on the immersed boundary or inside the body.

To solve the governing equations (2.1) and (2.2), a semi-implicit fractional step method is used (Spalart, Moser & Rogers, 1991):

$$\frac{\hat{u}_i^k - u_i^{k-1}}{\Delta t} = -\frac{2\alpha_k}{\rho_\varphi}\frac{\partial p^{k-1}}{\partial x_i} + \alpha_k[L(\hat{u}_i^k) + L(u_i^{k-1})] - \beta_k N(u_i^{k-1}) - \gamma_k N(u_i^{k-2}) + f_i^k, \tag{2.3}$$

$$\frac{\partial^2 \phi^k}{\partial x_i \partial x_i} = \frac{1}{2\alpha_k \Delta t}\left(\frac{\partial \hat{u}_i^k}{\partial x_i} - q^k\right), \tag{2.4}$$

$$u_i^k = \hat{u}_i^k - 2\alpha_k \Delta t \frac{\partial \phi^k}{\partial x_i}, \tag{2.5}$$

$$p^k = p^{k-1} + \rho_\varphi \phi^k - \mu_\varphi \alpha_k \Delta t \frac{\partial^2 \phi^k}{\partial x_j \partial x_j}, \tag{2.6}$$

with

$$L(u_i) = \nu_\varphi \frac{\partial^2 u_i}{\partial x_j \partial x_j}, \quad N(u_i) = \frac{\partial}{\partial x_j} u_i u_j, \tag{2.7}$$

where $\hat{u}_i$ are the intermediate velocity components and ϕ is the pseudo-pressure. Here, $k(= 1, 2, 3)$ is the substep index of a third-order Runge–Kutta method, $\alpha_1 = 4/15, \alpha_2 = 1/15, \alpha_3 = 1/6, \beta_1 = 8/15, \beta_2 = 5/12, \beta_3 = 3/4, \gamma_1 = 0, \gamma_2 = -17/60$, and $\gamma_3 = -5/12$. In the linear term, ν_φ is the kinematic viscosity of water or air. A third-order Runge–Kutta method is adopted for convection terms and the Crank–Nicolson method is used for viscous terms. The present numerical simulation is based on a finite-volume method on a staggered grid system (u_i are located at the cell faces, whereas p is located at the cell center). All the spatial derivatives are discretized with the second-order central difference scheme except that the one-side difference scheme is used at the wall and interface.

2.2 Computational details

Figure 2.1 shows the flow geometry and coordinate system of (a) the channel with no-slip walls and (b) the channel with SHSs. The SHSs are positioned on the both upper and lower channel walls. To match the experimental condition where the SHS is flush-mounted, the water height H is fixed and the geometric parameters of SHS are varied. The computational domain size (L_x, L_y, L_z) and the number of grid points (N_x, N_y, N_z) is given in chapters 3 and 4. Periodic boundary conditions are used in the streamwise and spanwise directions, and the no-slip condition is applied to both the upper and lower walls.

The computations are carried out by maintaining a constant mass flow rate in water flow for a Reynolds number $(Re = u_b H/\nu_l)$ of 5600 based on the water bulk velocity u_b, the water height H and the kinematic viscosity of water ν_l. This Reynolds number considered corresponds to $Re_{\tau_o} \simeq 180$ based on the wall-shear velocity of no-slip channel flow u_{τ_o}, where $u_{\tau_o} = \sqrt{\tau_w/\rho_l}$, τ_w is the mean wall-shear stress of no-slip channel flow. For precisely keeping a constant mass flow rate, Π_l is determined by obtaining the mean and fluctuating pseudo-pressure gradients separately at each time step (see You, Choi & Yoo (2000) for more details). All simulations are started with the fully developed velocity field with no-slip wall for the turbulent flow.

2.2.1 Boundary condition at the air-water interface

In the present simulation, some ideal circumstances are assumed by that (i) the air-water interface is flat and thus the surface tension effect is neglected, and (ii) there is no air dissolution into water. While the air-water interface is assumed to be flat, the wall-parallel velocities and shear stresses are maintained

to be continuous across the interface:

$$u_{l,s} = u_{g,s}, \qquad w_{l,s} = w_{g,s}, \tag{2.8}$$

and

$$\mu_l \frac{\partial u_l}{\partial y}\bigg|_s = \mu_g \frac{\partial u_g}{\partial y}\bigg|_s, \qquad \mu_l \frac{\partial w_l}{\partial y}\bigg|_s = \mu_g \frac{\partial w_g}{\partial y}\bigg|_s. \tag{2.9}$$

Here, the subscript 's' is the values at the interface. The wall-normal velocity at the interface is zero for satisfying an impermeability condition:

$$v_s = 0. \tag{2.10}$$

In the staggered grid system, the slip velocities are determined by the velocity components near the interface (see Fig 2.2). Using the one-side difference scheme at the interface, the slip velocities in the wall-parallel directions are following as

$$u_s = \frac{1}{1+\mu_R \Delta y_R} u_J + \frac{\mu_R \Delta y_R}{1+\mu_R \Delta y_R} u_{J+1}, \tag{2.11}$$

and

$$w_s = \frac{1}{1+\mu_R \Delta y_R} w_J + \frac{\mu_R \Delta y_R}{1+\mu_R \Delta y_R} w_{J+1}, \tag{2.12}$$

respectively, where $\mu_R = \mu_l/\mu_g$ and $\Delta y_R = \Delta y_J/\Delta y_{J+1}$. Note that Eqs. (2.11) and (2.12) are only valid at the lower air-water interface. For the upper interface, u_J and w_J, respectively, should be exchanged with u_{J+1} and w_{J+1}.

The boundary condition of pressure at the interface is derived from the momentum equation in the wall-normal direction (Eq. 2.1) and the $y-$momentum

equation at the interface is as following:

$$\rho_\varphi \left(\frac{\partial v_s}{\partial t} + u_s \frac{\partial v}{\partial x}\bigg|_s + v_s \frac{\partial v}{\partial y}\bigg|_s + w_s \frac{\partial v}{\partial z}\bigg|_s \right) = -\frac{\partial p}{\partial y}\bigg|_s + \mu_\varphi \left(\frac{\partial^2 v}{\partial x^2}\bigg|_s + \frac{\partial^2 v}{\partial y^2}\bigg|_s + \frac{\partial^2 v}{\partial z^2}\bigg|_s \right). \tag{2.13}$$

Since the wall-normal velocity at the interface is zero ($v_s = 0$), $\partial v_s/\partial x$ and $\partial v_s/\partial z$ are zero. Using the continuity ($\partial u/\partial x + \partial v/\partial y + \partial w/\partial z = 0$) and the commutative law, then, Eq. (2.13) is rewritten as

$$\frac{\partial p}{\partial y}\bigg|_s = -\mu_\varphi \left(\frac{\partial}{\partial x}\left(\frac{\partial u}{\partial y}\right)_s + \frac{\partial}{\partial z}\left(\frac{\partial w}{\partial y}\right)_s \right). \tag{2.14}$$

Finally, the boundary condition for the pressure at the interface is

$$\frac{\partial p_l}{\partial y}\bigg|_s = \frac{\partial p_g}{\partial y}\bigg|_s. \tag{2.15}$$

due to the matching condition of shear stresses at the interface (Eq. 2.9).

2.2.2 Flow type inside air layer

As Busse *et al.* (2013) and Tsai (2013) pointed out, the flow type inside the air layer of SHS has an influence on the slip length and skin-friction drag and it has to be prudently determined. In this thesis, three cases are considered as the flow inside the air layer. The first case (case 1) is that the flow inside air layer is under a shear rate induced by the air-water interface (as known as Couette flow, Joseph 1980; Vinogradova 1999). Π_g is zero, in case 1, since the air flow is shear-driven at the top of the air layer. The second case (case 2) is that the flow recirculates inside the air layer and thus its net mass flow rate is zero ($\dot{m}_g = 0$, Maynes *et al.* 2007; Busse *et al.* 2013). In case 2, Π_g is determined by the shear

stresses at the wall and interface as

$$\Pi_g = -\frac{\mu_g}{D}\left|\left(\frac{\partial \bar{u}_g}{\partial y}\right)_{wall} - \left(\frac{\partial \bar{u}_g}{\partial y}\right)_s\right|. \tag{2.16}$$

Note that a minus sign denotes the opposite direction to the mean pressure gradient of water flow ($\Pi_l > 0$). The last case (case 3) is that the air layer behaves the same as the water bulk flow under a streamwise mean pressure gradient ($\Pi_g = \Pi_l$), and this case is the traditional assumption for core-annular flow (Than, Rosso & Joseph, 1997; Tretheway & Meinhart, 2004) or stratified flow (Náraigh & Spelt, 2010; Govindarajan & Sahu, 2014). However, case 3 is not appropriate model for the SHS because the air layer is run out without *actively* continuous supply.

The effects of cases 1 (shear-driven flow, $\Pi_g = 0$) and 2 (recirculating flow with zero net mass flow rate, $\dot{m}_g = 0$) on the slip length and skin-friction reduction are discussed in Chapter 3, and case 1 ($\Pi_g = 0$) is only considered in Chapter 4.

2.2.3 Surface grating parameters

The representative supporting structures of SHS are ridges (or grooves) and posts. Cheng, Teo & Khoo (2009) investigated the effect of the configuration of SHS on the slip length using four different shapes: longitudinal grooves, transverse grooves, square posts, and square holes. They found that the SHS with longitudinal grooves has the largest slip length in laminar channel flow when the gas fraction (to be defined below) is up to 90% at low Reynolds numbers ($Re = 1$). At high Reynolds numbers ($Re > 300$), the SHS with longitudinal grooves has the largest slip length irrespective of the gas fraction. For turbulent flows, Daniello, Waterhouse & Rothstein (2009) and Park, Sun & Kim (2014)

successfully reduced the friction drag using SHSs with longitudinal grooves. Therefore, the longitudinal grooves is considered as the surface geometry in the present study.

The surface grating parameters considered are the pitch length ($L_p = L_s + L_g$), the gas fraction ($\phi = L_g/L_p$), and the air-layer thickness (D), where L_s and L_g are the width of longitudinal ridge and groove, respectively. The computational domain size (L_x, L_y, L_z) and the number of grid points (N_x, N_y, N_z) is given in each chapters. Periodic boundary conditions are used in the streamwise and spanwise directions, and the no-slip condition is applied to both the upper and lower walls.

2.2.4 Interface sustainability and deformability

In the present study, the air-water interface is assumed to be flat. According to Teo & Khoo (2009), the pressure difference between the air and water is significantly smaller than the capillary pressure, so that the curvature effects can be neglected in laminar flows. For turbulent flows, Seo *et al.* (2015) investigated the effect of the surface geometry (i.e. longitudinal grooves vs. square posts) on pressure fluctuations at the interface and suggested a relationship between the slip velocity and the root-mean-square (r.m.s) pressure fluctuations at the interface. Especially, Türk *et al.* (2014) and Seo *et al.* (2015) examined the sustainability of the interface between water and air against turbulent pressure fluctuations. They showed that the maintenance of the air-water interface depends on the pattern sizes of SHSs, and reported that the maximum sizes of the longitudinal grooves and square posts for its maintenance are about 150 and 50 wall units, respectively. Seo *et al.* (2015) also showed that the interface deformation by turbulent pressure fluctuations is negligible when the pattern

size of SHS is equal to 6 wall units with the capillary number of $Ca = 6 \times 10^{-3}$, where $Ca = \mu_l u_\tau / \sigma$, μ_l is the water viscosity, u_τ is the shear velocity, and σ is the surface tension between air and water ($\sigma = 0.073$ N/m). Piao & Park (2015) modeled pressure fluctuations at the interface as a harmonic oscillation and suggested that the pattern size of SHS should be $O(\mu\text{m})$ for the air-water interface to be stable.

2.3 Solution of laminar flow with SHS

The computational code for the present study was initially based on the channel flow with no-slip wall and validated by comparing with numerical data of Kim, Moin & Moser (1987) (not shown in this thesis). To validate the computational code for two-phase flows in the channel, DNS of laminar channel flow having the SHS are conducted with comparing the analytical solutions. (There is no comparable data for a turbulent flow). Here, the Reynolds numbers considered are 400 and 1200, but there is no sensible discrepancy. Since the streamwise uniformity ensures that all nonlinear terms do not influence the resulting flow field, there was no dependency of Reynolds number in laminar flow (Choi, Moin & Kim, 1991; Türk *et al.*, 2014). Hence the results for one Reynolds number are shown for laminar flow.

2.3.1 Laminar channel flow with an idealized SHS

In the fully-developed laminar channel flow with an idealized SHS (i.e., without any texture), there is a single non-zero streamwise velocity component that varies only in the wall-normal direction. Then, the $x-$momentum equations of water and air are

$$\mu_l \frac{d^2 u_l(y)}{dy^2} = -\Pi_l \quad (|y| \leq H/2), \tag{2.17}$$

and

$$\mu_g \frac{d^2 u_g(y)}{dy^2} = -\Pi_g \quad (H/2 \leq |y| \leq H/2 + D). \tag{2.18}$$

Here, the centerline of channel in the wall-normal direction is located at $y = 0$. The solutions to (2.17) and (2.18) are accomplished by double integration with boundary conditions at the no-slip wall and the air-water interface. For case 1,

	u_s/u_b	b_{app}/H	DR
Case 1 ($\Pi_g = 0$)	$\dfrac{6\mu_R d}{1+6\mu_R d}$	$\mu_R d$	$\dfrac{6\mu_R d}{1+6\mu_R d}$
Case 2 ($\dot{m}_g = 0$)	$\dfrac{6\mu_R d/4}{1+6\mu_R d/4}$	$\mu_R d/4$	$\dfrac{6\mu_R d/4}{1+6\mu_R d/4}$

Table 2.1. Key parameters of slip property.

$u_l(y)$ and $u_g(y)$, respectively, are

$$u_l(y) = \frac{\Pi_l H^2}{2\mu_l}\left[-\left(\frac{y}{H}\right)^2 + \frac{1}{4} + \mu_R d\right], \tag{2.19}$$

and

$$u_g(y) = \frac{\Pi_l H^2}{2\mu_g}\left[\mp\left(\frac{y}{H}\right) + \frac{1+2d}{2}\right], \tag{2.20}$$

and the velocity profiles for case 2 are

$$u_l(y) = \frac{\Pi_l H^2}{2\mu_l}\left[-\left(\frac{y}{H}\right)^2 + \frac{1}{4} + \frac{\mu_R d}{4}\right], \tag{2.21}$$

and

$$u_g(y) = \frac{\Pi_l H^2}{2\mu_g}\frac{1}{4d}\left[3\left(\frac{y}{H}\right)^2 \mp (3+4d)\left(\frac{y}{H}\right) + (3/4 + 2d + d^2)\right], \tag{2.22}$$

where $\mu_R(= \mu_l/\mu_g)$ is the viscosity ratio and $d(= D/H)$ is the air-layer thickness normalized by the water height. Note that Π_l of cases 1 and 2 are different from each other. For a constant mass flow rate in water flow, Π_l is $\Pi_o/(1+6\mu_R d)$ (case 1) or $\Pi_o/(1+6\mu_R d/4)$ (case 2), where Π_o is the mean pressure gradient of channel flow with no-slip wall.

From the velocity distribution of water flow, the slip velocity normalized by the bulk velocity (u_s/u_b), the apparent slip length normalized by the water height (b_{app}/H), and the DR rate are obtained and shown in Table 2.1. The DR rate is defined as

$$DR = \frac{\Pi_o - \Pi_l}{\Pi_o}, \tag{2.23}$$

and it has a positive value when the skin-friction drag decreases. As shown in Table 2.1, the DR rate is the same as the normalized slip velocity and they are rewritten with the slip length as $DR = u_s/u_b = 6b_{app}/(6b_{app} + H)$, regardless of the flow type inside the air layer.

Figure 2.3 shows the streamwise velocity profile with a constant mass flow rate in water. For both cases, the present numerical results are well-matched with the analytical solutions. Also, the important slip properties, such as the slip velocity, slip length, and DR rate, are well-estimated through the present numerical simulation as shown in Fig 2.4.

2.3.2 Laminar channel flow with SHS having longitudinal grooves

Inside the air layer of SHS with grooves, case 1 ($\Pi_g = 0$) is only considered and thus the $x-$momentum equations of water and air, respectively, are Poisson and Laplace equations:

$$\mu_l \left(\frac{\partial^2 u_l(y,z)}{\partial y^2} + \frac{\partial^2 u_l(y,z)}{\partial z^2} \right) = -\Pi_l, \tag{2.24}$$

and

$$\mu_g \left(\frac{\partial^2 u_g(y,z)}{\partial y^2} + \frac{\partial^2 u_g(y,z)}{\partial z^2} \right) = 0. \tag{2.25}$$

The coordinate system and boundary conditions are shown in Fig 2.5. According to Teo & Khoo (2009), $u_l(y,z)$ is decomposed as $u_l(y,z) = u_p(y) + \tilde{u}_l(y,z)$,

where $u_p(y)$ is the velocity component due to the Poiseuille flow with no-slip wall and $\tilde{u}_l(y,z)$ is that due to the presence of the SHS. $u_p(y)$ is well-known as

$$u_p(y) = \frac{\Pi_l H^2}{2\mu_l}\left[-\left(\frac{y}{H}\right)^2 + \frac{1}{4}\right], \tag{2.26}$$

and $\tilde{u}_l(y,z)$ can be expressed as Fourier cosine series (Teo & Khoo, 2009):

$$\tilde{u}_l(y,z) = A + \sum_{n=1}^{\infty} B_n \cosh\left(\frac{n\pi}{L_p}y\right)\cos\left(\frac{n\pi}{L_p}z\right), \tag{2.27}$$

where

$$A = \frac{1}{L_g}\int_{-L_g/2}^{L_g/2} u_s(z)dz, \tag{2.28}$$

and

$$B_n = \frac{2}{L_g\cosh(n\pi/L_g(H/2))}\int_{-L_g/2}^{L_g/2} u_s(z)\cos\frac{n\pi z}{L_g}dz. \tag{2.29}$$

Eq. (2.27) is valid in the range of $-L_g/2 \le z \le L_g/2$.

To solve Eq. (2.25), the coordinate transform is performed inside the air layer as $y^* = y + D + H/2$ and $z^* = z + L_g/2$. Using the Fourier sine series, $u_g(y^*, z^*)$ is

$$u_g(y^*, z^*) = \sum_{n=1}^{\infty} C_n \sinh\left(\frac{n\pi}{L_g}y^*\right)\sin\left(\frac{n\pi}{L_g}z^*\right), \tag{2.30}$$

where

$$C_n = \frac{2}{L_g\sinh(n\pi D/L_g)}\int_0^{L_g} u_s(z^*)\sin\frac{n\pi z^*}{L_g}dz^*. \tag{2.31}$$

Eqs. (2.27) and (2.30) are given in terms of the slip velocity $u_s(z)$. The slip velocity $u_s(z)$ is unknown yet and thus the velocity distributions in air and water are underdetermined. Therefore, other approach to validate the present numerical code is required.

Belyaev & Vinogradova (2010) proposed the theorectical formula for the effective slip length as

$$b_{eff} = \frac{\dfrac{L_p}{\pi} \ln \left[\sec \left(\dfrac{\pi\phi}{2} \right) \right]}{1 + \dfrac{L_p}{\pi \tilde{b}} \ln \left[\sec \left(\dfrac{\pi\phi}{2} \right) + \tan \left(\dfrac{\pi\phi}{2} \right) \right]}, \tag{2.32}$$

where $\tilde{b}$ is a local slip length at the air-water interface. Since the slip velocity is a function of z, $\tilde{b}$ may be varied in the z-direction as well. However, Belyaev & Vinogradova (2010) assumed $\tilde{b}$ as a constant slip length, b_{app}, which is determined by only the air-layer thickness. Here, b_{app} is considered as $\mu_R D$ (see Table 2.1). By the numerical simulation, b_{eff} is obtained and compared with Eq. (2.32).

Figure 2.6 shows the variation of the effective slip length with the surface geometry. The pitch lengths, the gas fractions, and the air-layer thicknesses are varied from $0.09375H$ to H, 0.25 to 0.75, and $0.005H$ to $0.05H$, respectively. With increasing the surface grating parameters, the effective slip length increases. The deviation between the present slip length and that by Belyaev & Vinogradova (2010) is determined as

$$e = \frac{b_{eff}(\text{present}) - b_{eff}(\text{Belyaev \& Vinogradova})}{b_{eff}(\text{present})}. \tag{2.33}$$

Figure 2.7 shows that the present numerical data have a good agreement with that of the analytical formula although the error is accompanied by the assumption of a constant slip at the interface.

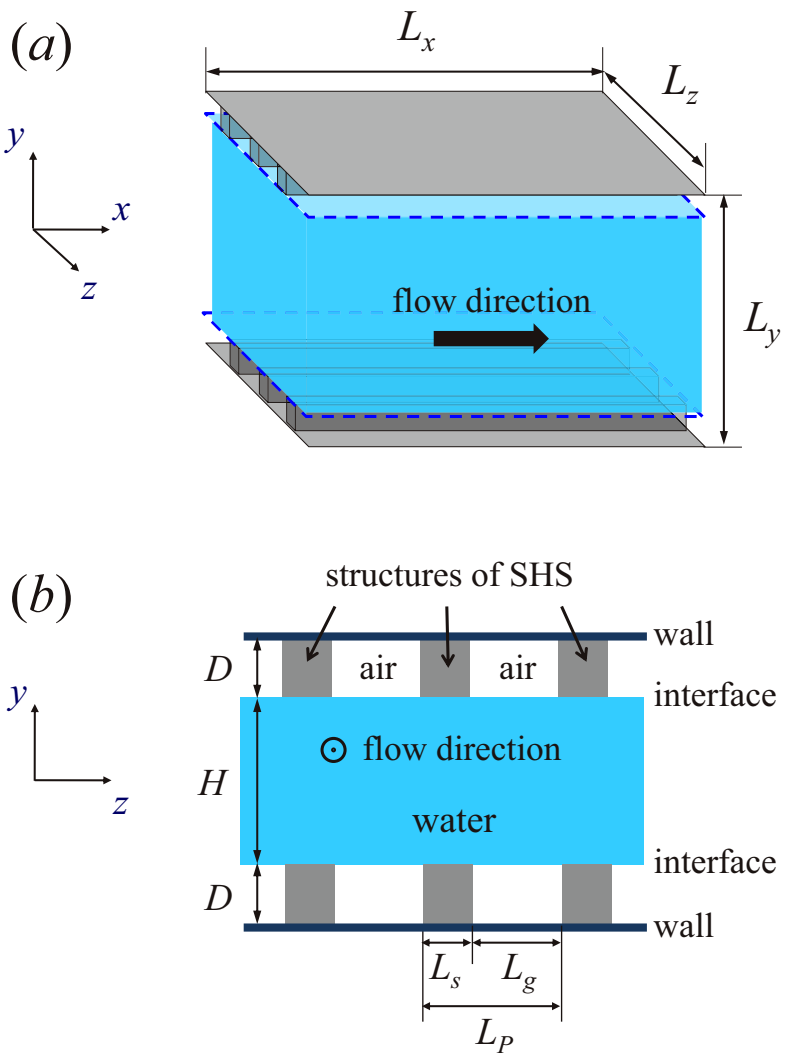

Figure 2.1. Schematic diagrams: (a) perspective view; (b) end view. Here, H and D are the water height and air-layer thickness, respectively. L_s, L_g, and L_p are the width of longitudinal ridge and groove, and the pitch length, respectively.

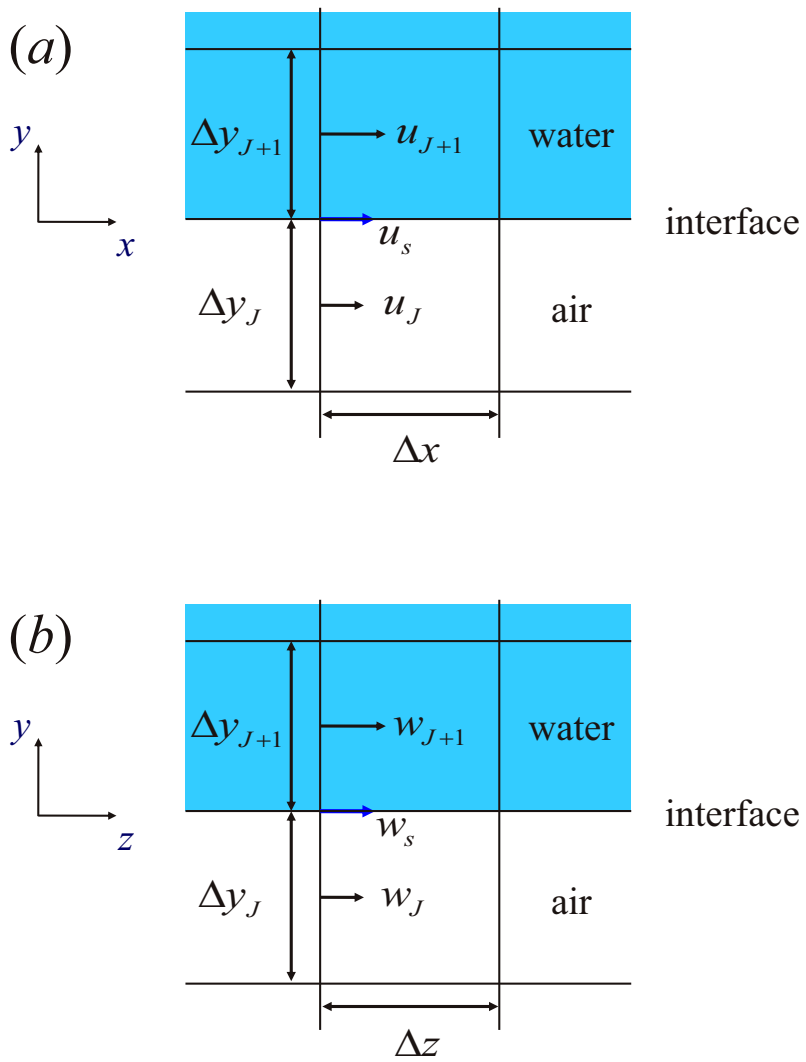

Figure 2.2. Slip velocity at the lower air-water interface on the staggered mesh: (a) in the x-direction; (b) in the z-direction.

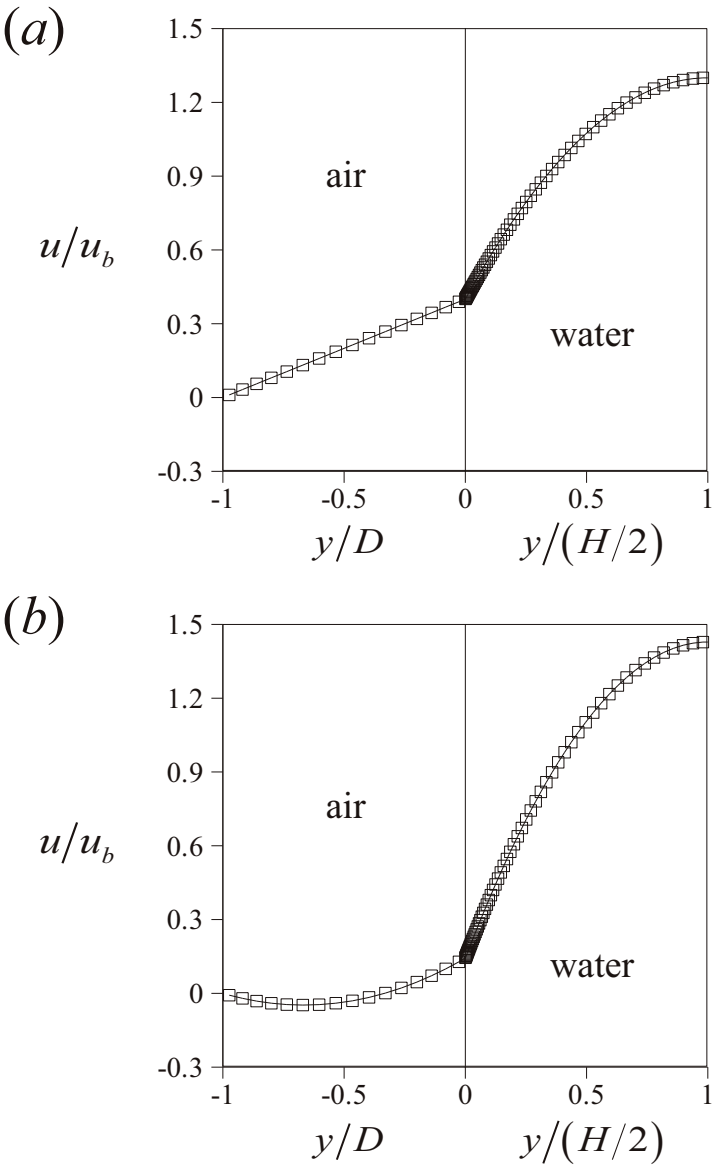

Figure 2.3. Velocity profiles in air and water ($D = 0.002H$): (a) case 1; (b) case 2. Symbol is the result of the numerical simulation and line is the analytical solution.

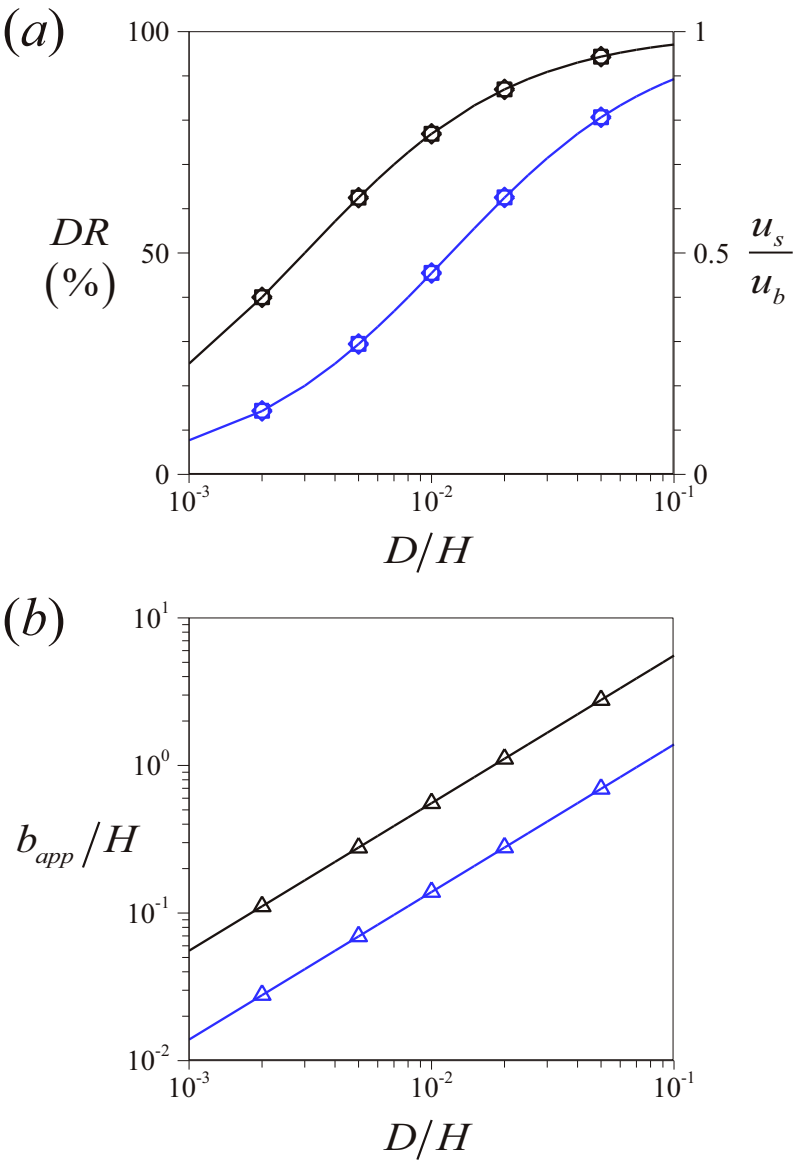

Figure 2.4. (a) Variation of the DR rate and slip velocity with the air-layer thickness; (b) Variation of the apparent slip length with the air-layer thickness: symbol, numerical data; line, analytical solution. Black and blue lines are cases 1 and 2, respectively. In (a), square and diamond, respectively, denote the DR rate and slip velocity.

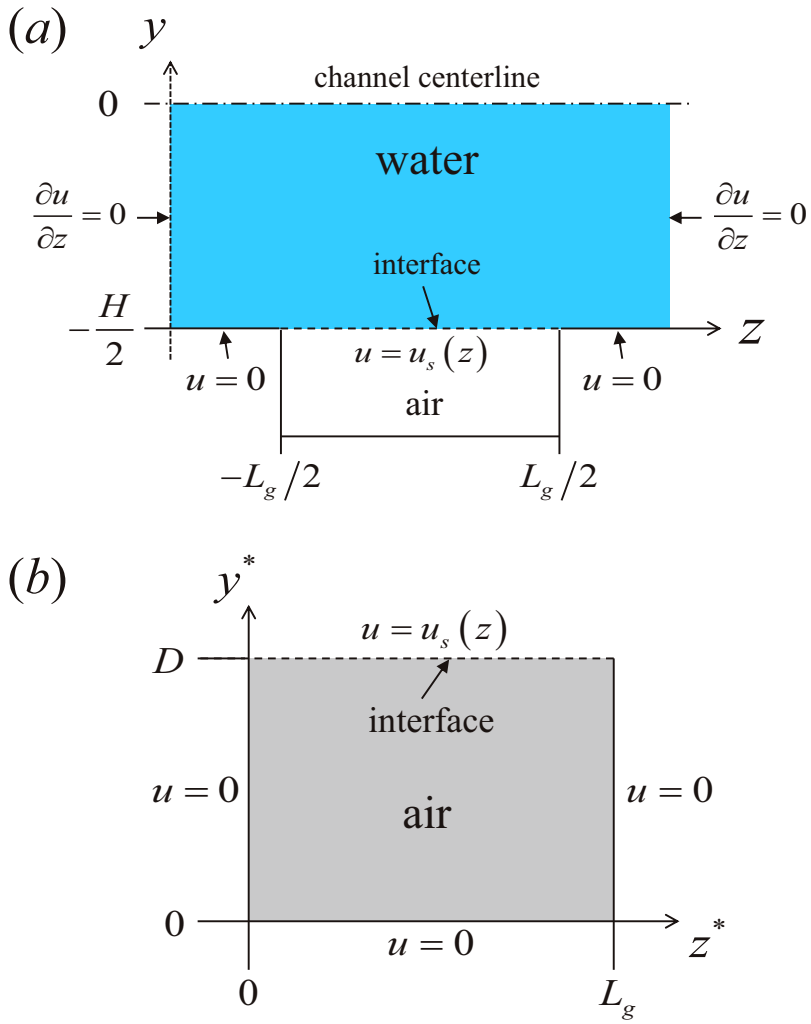

Figure 2.5. Flow geometry and given boundary values: (a) water region; (b) air region.

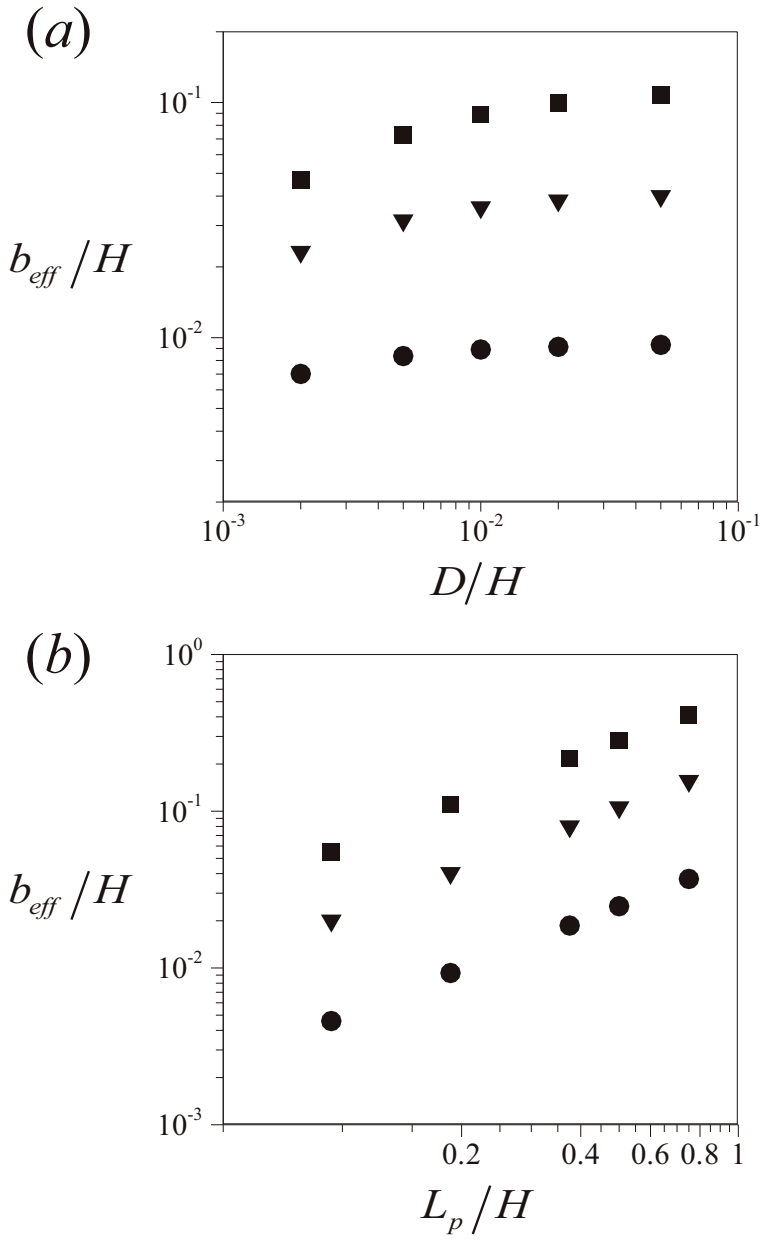

Figure 2.6. Variation of the effective slip length with (a) the air-layer thickness or (b) the pitch length. Symbols denote the gas fraction: square, $\phi = 0.75$; gradient, $\phi = 0.5$; circle, $\phi = 0.25$.

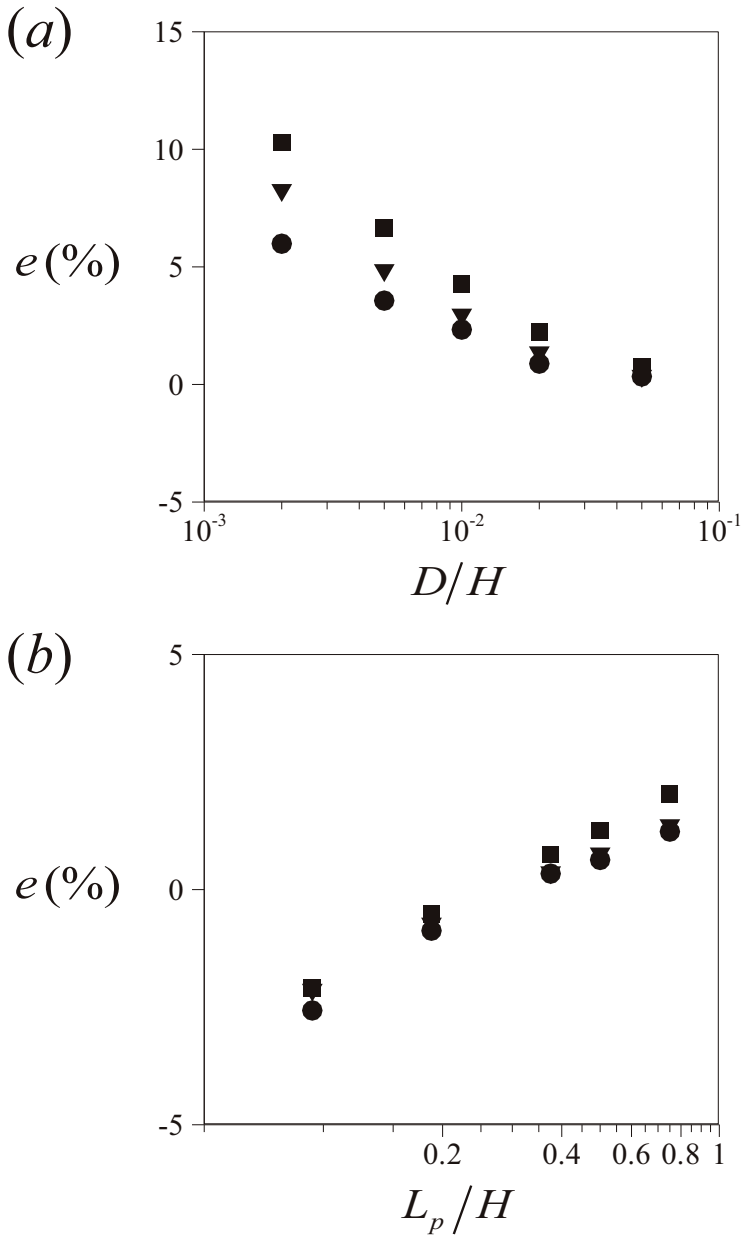

Figure 2.7. Variation of the deviation between numerical data and analytical solution (Belyaev & Vinogradova, 2010) with (a) the air-layer thickness or (b) the pitch length. Symbols denote the gas fraction: square, $\phi = 0.75$; gradient, $\phi = 0.5$; circle, $\phi = 0.25$.

Chapter 3

Turbulent channel flow with an idealized superhydrophobic surface

3.1 Introduction

In this chapter, I perform DNS of turbulent channel flow by solving both the main water flow and the air-layer flow inside an idealized SHS. The word 'idealized' means that there is no pole or ridge inside the air layer. When the solid fraction of SHS is very small, this ideal assumption may be valid (Busse *et al.*, 2013). Even if this assumption is not realistic, one could obtain important flow properties at the air-water interface from the present problem setting.

The present results are compared with those from previous studies using the Navier slip model without solving the air layer that provides slip velocities in the streamwise and spanwise directions at the air-water interface as $u_s = b_x(\partial u/\partial y)_s$ and $w_s = b_z(\partial w/\partial y)_s$, where b_x and b_z are the streamwise and spanwise slip lengths, and $(\partial u/\partial y)_s$and $(\partial w/\partial y)_s$ are the streamwise and spanwise shear rates at the interface, respectively (Hahn, Je & Choi, 2002; Min & Kim, 2004; Fukagata, Kasagi & Koumoutsakos, 2006; Busse & Sandham, 2012). The main weakness of this slip model is that the slip lengths b_x and b_z are unknown, and thus they have to be prescribed *a priori*. On the other hand, in the present simulation with the air layer, the slip lengths b_x and b_z

are obtained *a posteriori* from the results of direct numerical simulation. Then, the anisotropy of the slip lengths in the streamwise and spanwise directions, i.e. $b_x \neq b_z$, and its effect on the skin-friction reduction are examined in detail.

3.2 Computational details

The flow geometry and coordinate system are shown in figure 3.1, where H is the water height and D is the air-layer thickness. In the present simulation, I assume that (i) the air-water interface is flat and thus the surface tension is neglected, (ii) there is no air dissolution into water, and (iii) there is no ridge or pole inside the air layer. When the gap of supporting structures and the solid fraction of SHS are small, the assumptions (i) and (iii) may be valid (Busse *et al.*, 2013; Seo *et al.*, 2015). I fix H and vary D to match the experimental condition where the SHS is flush-mounted.

Two different flow types inside the air layer are considered: in case 1, the flow inside the air layer is shear-driven at the air-water interface (Joseph, 1980; Vinogradova, 1999); in case 2, the flow recirculates inside the air layer and thus its net mass flow rate is zero (Maynes *et al.*, 2007; Busse *et al.*, 2013). In both cases, the analytical solutions of laminar flow are obtained in §2.3.

The unsteady incompressible Navier-Stokes and continuity equations are solved in both water and air flows. The wall-parallel velocities and shear stresses are continuous across the air-water interface, while the interface is assumed to be flat. Uniform grids are used in the streamwise and spanwise directions and the grid spacings in wall units are $\Delta x^{+o} \approx 8$ and $\Delta z^{+o} \approx 4$. In the wall-normal direction, non-uniform grids are constructed by using a hyperbolic tangent function ($\Delta y^{+o} \approx 0.2 \sim 7$ for water and $\Delta y^{+o}_{min} \approx 0.01 \sim 0.2$ for air). All simulations are started from a fully developed turbulent channel flow with no-slip wall. The air-layer thicknesses (D) considered are from $0.0002H$ to $0.05H$. The initial turbulent flow becomes laminar for $D \geq 0.005H$ (case 1) and $D \geq 0.02H$ (case 2), so the cases up to $D < 0.005H$ (case 1) and $D < 0.02H$ (case 2) are discussed in this thesis.

3.3 Results

3.3.1 Apparent slip length and skin-friction reduction

The apparent slip length (or Navier slip length) is obtained from $b_{app} = \bar{u}_s/(\partial\bar{u}_l/\partial y)_s$, where $\bar{u}_s$ is the mean slip velocity and $(\partial\bar{u}_l/\partial y)_s$ is the mean velocity gradient of water at the interface. Figure 3.2 shows the variation of the apparent slip length with the air-layer thickness. For both cases 1 and 2, the apparent slip lengths linearly increase with the air-layer thickness and their slopes are μ_R and $\frac{1}{4}\mu_R$, respectively, where μ_R is the viscosity ratio ($\mu_R = \mu_l/\mu_g$). At a given air-layer thickness, more slip is induced by the shear-driven air flow (case 1) than by the recirculating air flow (case 2). It is interesting to note that the apparent slip length of turbulent flow is the same as that of laminar flow. This counter-intuitive result can be explained by the definition of the apparent slip length. The apparent slip length is rewritten as $b_{app} = \mu_R\bar{u}_s/(\partial\bar{u}_g/\partial y)_s$ by matching the shear stresses at the air-water interface. When the velocity profiles inside the air layer are the linear (case 1) and quadratic (case 2) functions, $(\partial\bar{u}_g/\partial y)_s$'s are $\bar{u}_s/D$ and $4\bar{u}_s/D$ for cases 1 and 2, respectively. Then, the apparent slip length depends only on μ_R and D, independent of the flow condition in water. The mean velocity profiles of air layer are indeed linear and quadratic for cases 1 and 2, respectively (see below). The apparent slip length in the viscous wall unit ($b^{+_o} = b_{app}u_{\tau_o}/\nu_l$) in figure 3.2 shows that relaminarization starts when $b^{+_o} \geq 100$ in both cases. This is consistent with the observation by Busse & Sandham (2012).

Figure 3.3 shows the variations of the DR rate and mean slip velocity with the air-layer thickness, where the DR rate is defined as $DR = (\Pi_o - \Pi_l)/\Pi_o$, Π_o is the mean pressure gradient with the no-slip wall. As the air-layer thickness increases, the DR rate and mean slip velocity also increase. Although the DR

rate is equal to the slip velocity in laminar flow (Rastegari & Akhavan, 2015), the DR rate is larger than the mean slip velocity in turbulent flow and also than that of laminar flow. This is because the DR of turbulent flow is determined by the combination of pure slip effect and weakening of near-wall turbulence (Park, Park & Kim, 2013; Rastegari & Akhavan, 2015).

Figure 3.4 shows the variations of the DR rate with the slip length normalized by u_{τ_o} and ν_l, together with two empirical formulas for the relationship between the DR rate and the normalized slip length. These empirical formulas based on the log-law of Dean's formula (Dean, 1978) are proposed by Fukagata, Kasagi & Koumoutsakos (2006) and Busse & Sandham (2012) as

$$\begin{aligned}&\frac{1}{\kappa}\ln Re_{\tau_o} + F_o \\ &= (1-DR)b_x^{+o} + \sqrt{1-DR}\left[\frac{1}{\kappa}\ln(Re_{\tau_o}\sqrt{1-DR}) + F(b_z^{+o}\sqrt{1-DR})\right]\end{aligned} \tag{3.1}$$

where $\kappa = 0.41$ and $F_o = 3.2$, and b_x and b_z are the slip lengths for the velocity fluctuation components in the wall-parallel directions. In equation (3.1), the first and second terms of the right hand side are derived by considering the streamwise slip only ($b_z = 0$). The function $F(b_z, DR)$ in the last term of the equation is an empirical function describing the drag increase by the spanwise slip. Fukagata, Kasagi & Koumoutsakos (2006) and Busse & Sandham (2012), respectively, proposed the empirical function F from their DNS data as

$$F(b_z^{+o}) = F_\infty + (F_o - F_\infty)\exp\left[-(b_z^{+o}/a)^b\right], \tag{3.2}$$

or

$$F(b_z^{+o}) = F_\infty + \frac{(F_o - F_\infty)^2}{(F_o - F_\infty) + b_z^{+o}} \tag{3.3}$$

where $a = 7$, $b = 0.7$, and $F_\infty = -0.8$. Note that the abscissa in figure 3.4 is the normalized apparent slip length ($b^{+o} = b_{app}u_\tau/\nu_l$). The present DR rate falls in between the empirical formulas for the streamwise slip only ($b_z = 0$, Fukagata, Kasagi & Koumoutsakos 2006) and isotropic slip ($b_x = b_z$, Fukagata, Kasagi & Koumoutsakos 2006 and Busse & Sandham 2012), indicating (see below) that the present idealized SHS with an air layer generates an anisotropic slip ($b_x \neq b_z$) and more slip in the streamwise direction than in the spanwise one ($b_x > b_z$).

3.3.2 Anisotropic slip at the air-water interface

Figure 3.5 shows the modified mean velocity profiles in the viscous wall unit, $\bar{u}^+ - \bar{u}_s^+$, except inside the air layer, where $y^+ = 0$ is the location of the air-water interface. Here, the superscript + denotes the value normalized by the shear velocity at the interface (u_τ). As the air-layer thickness increases, the modified mean velocity shifts downward in the buffer and log layers (note that the mean velocity itself shifts upward with increasing air-layer thickness). Min & Kim (2004) reported that these mean velocities fall on one curve for streamwise slip only, but show downward shifts for combined streamwise and spanwise slip, indicating that the present interface has non-negligible spanwise slip.

To further investigate the nature of the slip at the interface, I examine the relation between the slip velocity and velocity gradient at the interface. Figure 3.6 shows the joint probability density functions (PDFs) between the instantaneous streamwise slip velocity and velocity gradient at the interface for both cases. The slope between these two (normalized) variables is near 1 for both cases 1 and 2, although this slope becomes lower for larger D/H. These results mean that $u_s \sim \mu_R D(\partial u_l/\partial y)_s$ or $b_x \sim \mu_R D$ for both cases. This result is

surprising, because the apparent slip lengths for cases 1 and 2 are $b_{app} = \mu_R D$ and $\mu_R D/4$ (or $\bar{u}_s = \mu_R D(\partial \bar{u}_l/\partial y)_s$ and $\bar{u}_s = \frac{1}{4}\mu_R D(\partial \bar{u}_l/\partial y)_s$), respectively (see figure 3.2). As shown in figure 3.6 (solid circles), the slip lengths between the mean slip velocities and mean velocity gradients hold for the present two cases in terms of joint PDF. The present results clearly indicate that the slip length used for the mean slip velocity and interface velocity gradient should not be applied to instantaneous ones (or fluctuating quantities). Rather, for the two cases considered here, the slip length of $b_x = \mu_R D$ may be applied to the fluctuating components. Thus, the instantaneous streamwise slip velocity may be modeled as (unless the DR rate is very large)

$$u_s = \begin{cases} \mu_R D \left(\dfrac{\partial u_l}{\partial y}\right)_s & \text{for case 1} \\ \mu_R D \left(\dfrac{\partial u_l}{\partial y}\right)_s - \dfrac{3}{4}\mu_R D \left(\dfrac{\partial \bar{u}_l}{\partial y}\right)_s & \text{for case 2.} \end{cases} \tag{3.4}$$

Figure 3.7 shows the joint PDFs between the instantaneous spanwise slip velocity and velocity gradient at the interface for both cases, where the mean spanwise velocity is zero. From this result, the instantaneous spanwise slip velocity may be modeled as

$$w_s = \frac{1}{4}\mu_R D \left(\frac{\partial w_l}{\partial y}\right)_s \quad \text{for cases 1 and 2,} \tag{3.5}$$

and $b_z = \mu_R D/4$. Thus, the slip effect in the spanwise direction is much weaker than that in the streamwise direction. The reason why the slip lengths for the streamwise and spanwise fluctuating velocities are different from each other is examined in §3.3.3.

The present slip-velocity model, equations (3.4) and (3.5), provides the

anisotropic slip-length relation of $b_z = b_x/4$. The DR rates versus the slip length with $b_z = b_x/4$ (using the formulas by Fukagata, Kasagi & Koumoutsakos (2006) and Busse & Sandham (2012)) are plotted in figure 3.8, showing excellent agreements with the present simulations results of case 1 but slight over-prediction for case 2. We also perform separate DNSs with the present model as the slip boundary conditions (without solving the air layer) and provide the results in figure 3.8. As shown, the present slip-velocity model successfully predicts the drag changes.

3.3.3 Flow structures in air and water

Figure 3.9 shows the mean velocity profiles in air and water for cases 1 and 2. As mentioned before, the mean velocity profiles inside the air layer are linear (case 1) and quadratic (case 2), and their slopes or curvatures increase with increasing air-layer thickness (note that their dimensional slopes ($\bar{u}_s/D$) or curvatures ($6\bar{u}_s/D^2$ at $\partial\bar{u}_g/\partial y$) decrease with increasing air-layer thickness. On the other hand, with increasing air-layer thickness, the mean velocity in water increases near the interface owing to the increased slip velocity but decreases near the centerline to maintain the same mass flow rate inside the channel. Figure 3.10 shows the root-mean-square (rms) velocity fluctuations normalized by u_{τ_o}. The rms velocity fluctuations are significantly reduced in water flow for both cases as the air-layer thickness increases. At the air-water interface, for case 1, the streamwise velocity fluctuations increase but the spanwise velocity fluctuations first increase and then decrease with increasing air-layer thickness, whereas for case 2, both the streamwise and spanwise velocity fluctuations first increase and then decrease.

The results shown in figures 3.6 and 3.7 indicate that the profiles of the

streamwise and spanwise velocity fluctuations inside the air layer are more like linear and quadratic, regardless of the cases considered here. In figure 3.11, some of the instantaneous streamwise and spanwise velocity fluctuations inside the air layer from the present simulations are plotted. This figure clearly shows that the profiles of streamwise velocity fluctuations are very different from those of spanwise velocity fluctuations, and the first is more like linear but the latter is quadratic. In the present case, the air layer is driven by the velocity on the liquid side. Similarly to no-slip turbulent channel flows, the near-interface structure (i.e. low-speed streak) should be elongated in the streamwise direction; which means that the air layer is oscillated at lower frequencies in the streamwise direction and higher frequencies in the spanwise direction. That difference in the driving frequency might have resulted in the difference in the shapes of velocity profiles as presented in figure 3.11 (see the solutions of the Stokes' second problem between two parallel plates for low and high frequency oscillations; Lamb (1916)).

Figure 3.12 shows the contours of the instantaneous streamwise vorticity on a cross-flow plane for no-slip wall and present SHSs. The air-layer thickness is $0.002H$ for both cases, but the slip length of case 1 ($b^+ = 19.6$) is much larger than that of case 2 ($b^+ = 7.4$). Therefore, near-wall vortical structures are much more weakened in case 1. It is noteworthy that turbulence structures are significantly weakened by the air layer (top and bottom) whose thickness is only 0.2% of the channel height.

Table 3.1 shows the Reynolds numbers based on the shear velocities at the interface in air and water, respectively, where the Reynolds numbers in air flow are defined as $Re_\tau = u_\tau D/\nu_g$ (case 1) and $u_\tau(D/2)/\nu_g$ (case 2), respectively. It is notable that the Reynolds numbers in air flow are less than 2 for all the cases considered. Therefore, turbulence in air flow hardly survives and

Case 1 ($\Pi_g = 0$)			Case 2 ($\dot{m}_g = 0$)			
D/H	Re_τ (water)	Re_τ (air)	D/H	Re_τ (water)	Re_τ (air, wall)	Re_τ (air, interface)
0.0002	154.7	0.12	0.001	153.3	0.21	0.29
0.0005	132.7	0.26	0.002	136.3	0.37	0.52
0.001	110.8	0.43	0.005	104.9	0.71	1.01
0.002	88.1	0.68	0.01	82.0	1.11	1.58

Table 3.1. Reynolds numbers based on the shear velocities in water and air.

dissipates although it is continuously supplied at the interface from water flow. Bech *et al.* (1995) reported that transition occurs in plane Couette flow at $Re_{Cou}(= \bar{u}_s D/\nu_g) \approx 1440$ and a fully developed turbulent flow is observed at $Re_{Cou} \geq 2000$. For the present case 1, $Re_{Cou} \approx 0.01 \sim 0.5$, which is much lower than that suggested by Bech *et al.* (1995) to maintain turbulence inside the air layer.

3.4 Summaries

In this chapter, I investigated the effects of the air layer on the slip length and skin-friction reduction. Two different flow types inside the air layer were considered: a shear-driven flow and a recirculating flow with zero net mass flow rate. For this purpose, the flow inside the air layer underneath the water turbulent flow was directly simulated with the assumption that the interface was flat (neglecting the surface tension effect). The slip length, slip velocity and drag reduction rate increased as the air-layer thickness increased. At a given air-layer thickness, the shear-driven flow in the air layer supplied more slip than the recirculating flow. However, when the slip length was the same, there seemed no clear difference in the drag reduction rate and slip velocity between two cases. The present drag reduction rate fell in between those from the streamwise slip only and isotropic slip, indicating that the present air-water interface generates an anisotropic slip (stronger in the streamwise slip than in the spanwise one). I showed that the Navier slip model should be applied to mean values only, and not to instantaneous (or fluctuating) quantities. In this regard, I proposed a new slip model (equations 3.4 and 3.5) that provides more slip in the streamwise direction than in the spanwise direction, and showed the validity of this model by separate direct numerical simulations. Finally, the rms velocity fluctuations and near-wall vortical structures in the water flow were significantly weakened by the air layer, but unsteady motions still existed inside the air layer.

An ideal circumstance (i.e., no supporting structures on SHS) was considered in this chapter. In reality, SHSs have a texture such as ridge or post and many previous studies reported the importance of the texture (Martell, Perot & Rothstein, 2009; Park, Park & Kim, 2013; Jelly, Jung & Zaki, 2014; Türk

et al., 2014; Seo *et al.*, 2015). This subject is to be investigated in the following chapter.

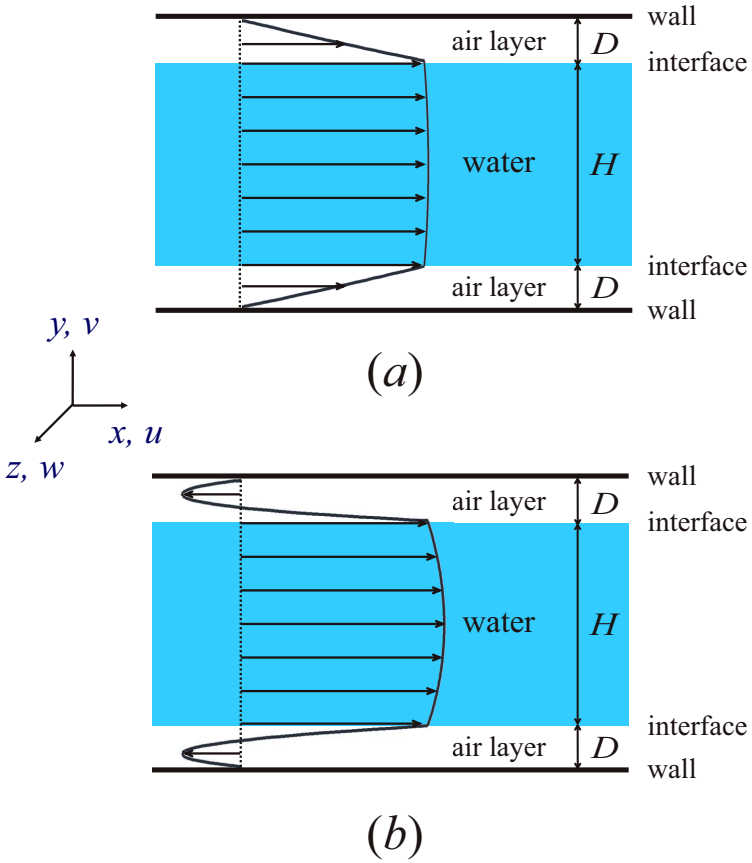

Figure 3.1. Flow geometry: (a) case 1 ($\Pi_g = 0$; shear-driven flow type in the air layer); (b) case 2 ($\dot{m}_g = 0$; recirculating flow type in the air layer). Here, Π_g is the source term for driving air flow and $\dot{m}_g$ is the mass flow rate within the air layer.

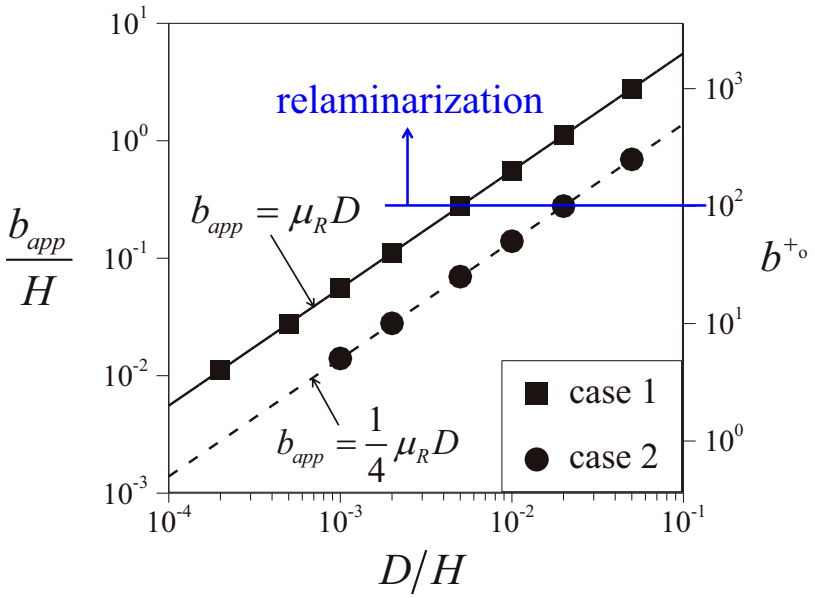

Figure 3.2. Variation of the slip length with the air-layer thickness: symbol, turbulent flow; line, laminar flow.

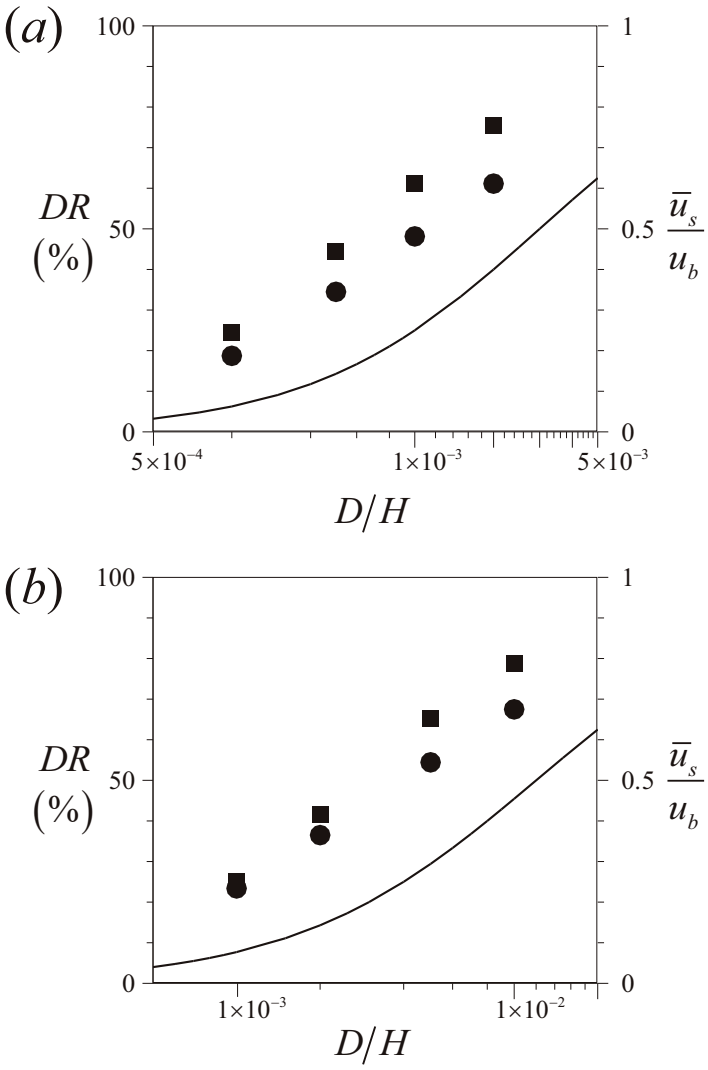

Figure 3.3. Variations of the DR rate and mean slip velocity with the air-layer thickness: square, DR rate; circle, mean slip velocity. Solid line is those of laminar flow.

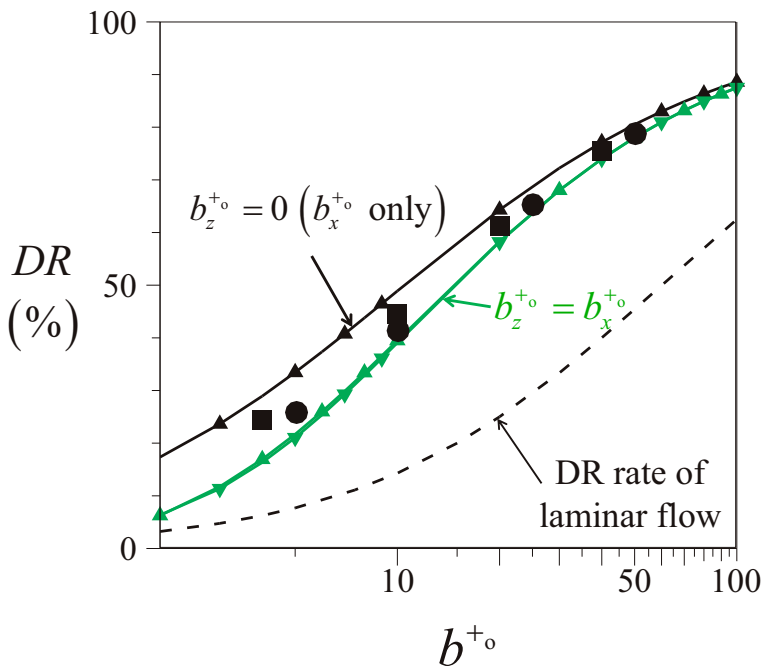

Figure 3.4. Variations of the DR rate with the apparent slip length in wall units. Solid lines are the DR rates by empirical formulas: b_x only, Fukagata, Kasagi & Koumoutsakos (2006); $b_x = b_z$, Fukagata, Kasagi & Koumoutsakos (2006) (line with triangles) and Busse & Sandham (2012) (line with inverse triangles). The black squares (case 1) and circles (case 2) denote the present DR rates with solving the air layer. The dashed line is the DR rate of laminar flow.

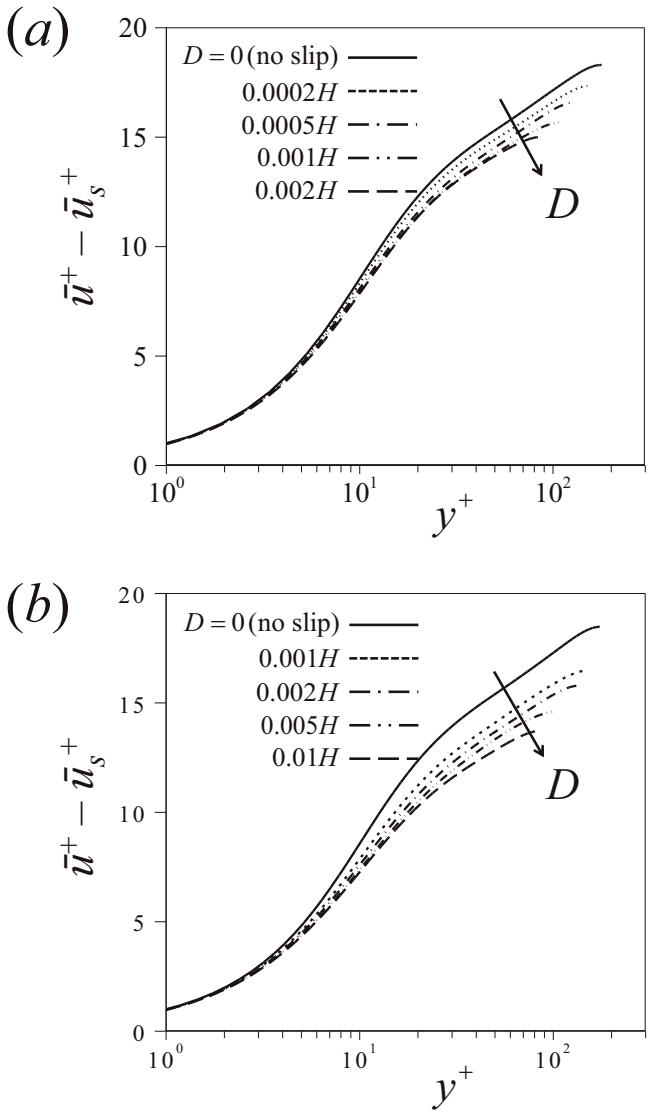

Figure 3.5. Modified mean velocity ($\bar{u}^+ - \bar{u}_s^+$) profiles normalized by their friction velocities at the interface: (a) case 1; (b) case 2.

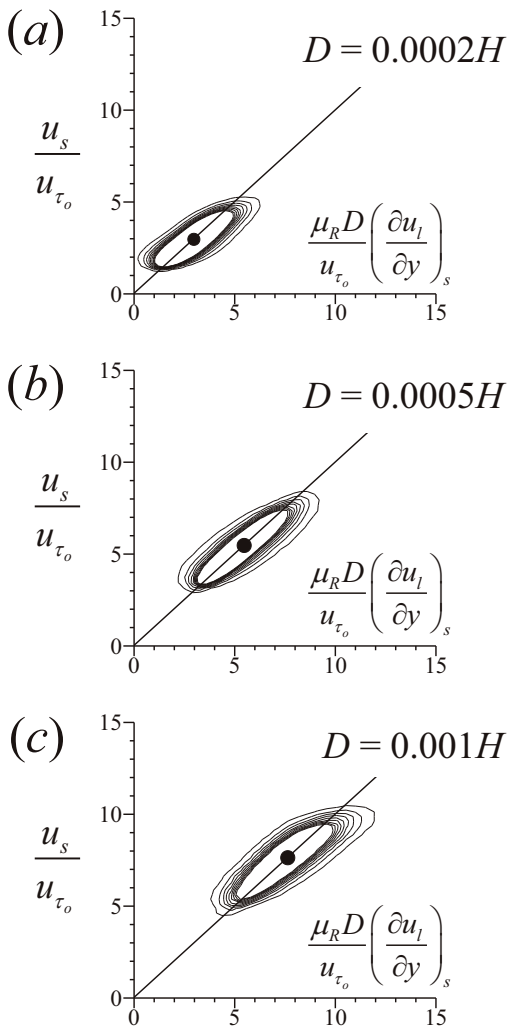

Figure 3.6. For caption, see the following page.

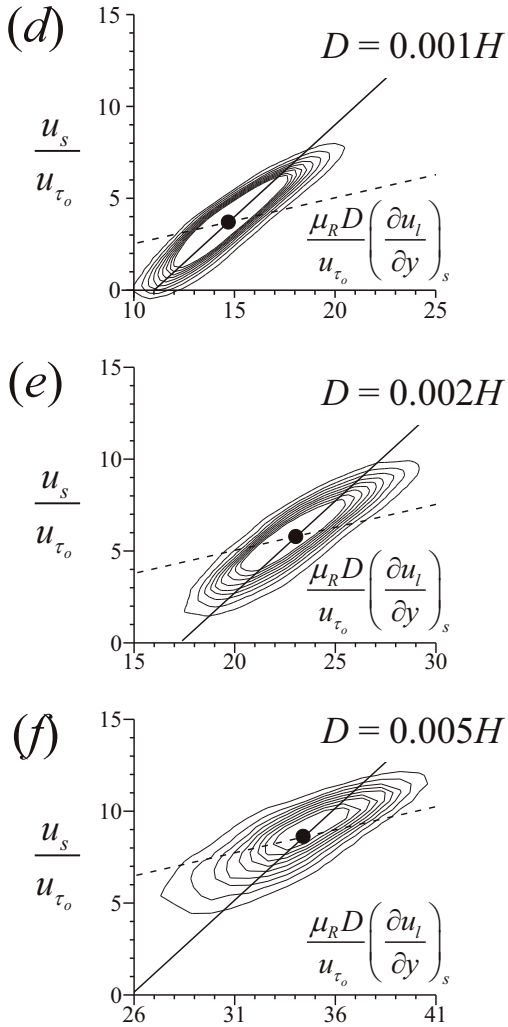

Figure 3.6. Joint probability density function of u_s vs. $(\partial u_l/\partial y)_s$: (a) - (c) case 1; (d) - (f) case 2. The contour levels are from 0.005 to 0.045 by increments of 0.005. The solid and dashed lines have the slopes of 1 and 1/4, respectively. The solid circles denote the mean values of the slip velocity and streamwise velocity gradient.

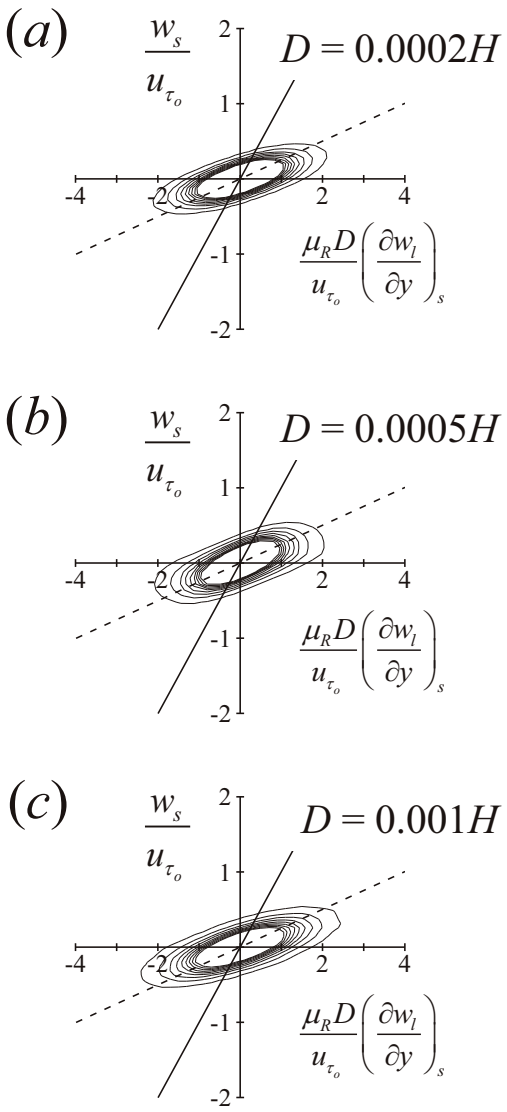

Figure 3.7. For caption, see the following page.

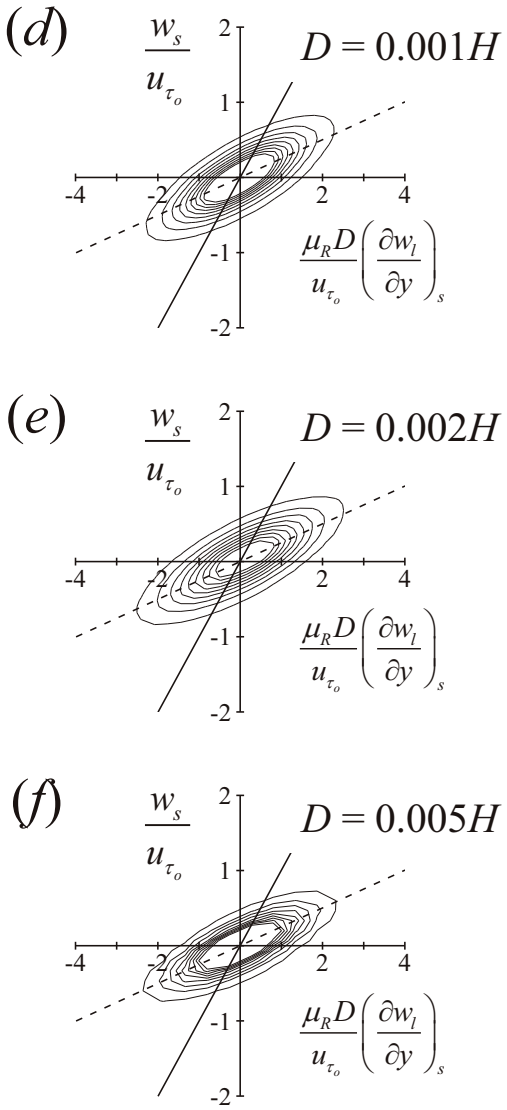

Figure 3.7. Joint probability density function of w_s vs. $(\partial w_l/\partial y)_s$: (a) - (c) case 1; (d) - (f) case 2. The contour levels are from 0.05 to 0.45 by increments of 0.05. The solid and dashed lines have the slopes of 1 and 1/4, respectively.

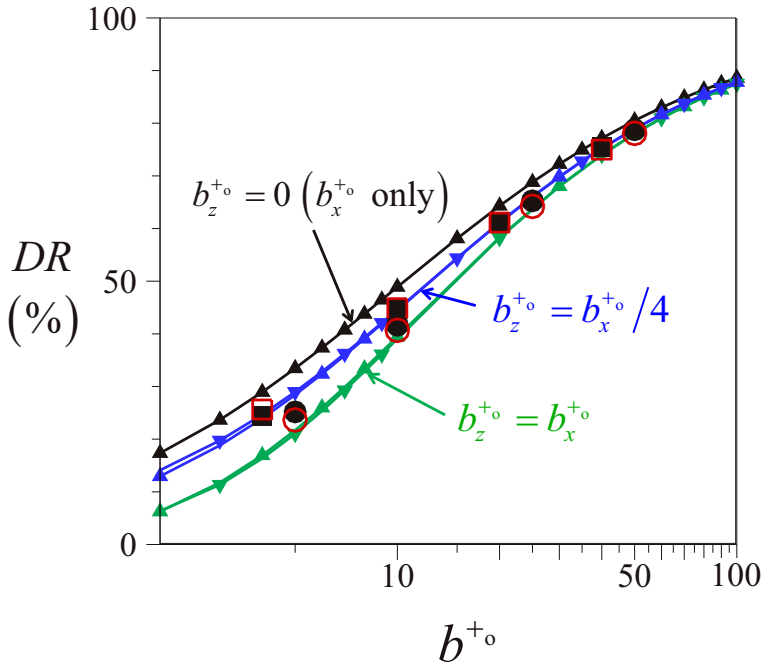

Figure 3.8. Variations of the DR rate with the apparent slip length in wall units. Solid lines are the DR rates by empirical formulas: lines with triangles, Fukagata, Kasagi & Koumoutsakos (2006); lines with inverse triangles, Busse & Sandham (2012). The black squares (case 1) and circles (case 2) denote the present DR rates with solving the air layer. The red open squares (case 1) and circles (case 2) denote the DR rates from DNS results with the present slip-velocity model, (3.4) and (3.5), without solving the air layer.

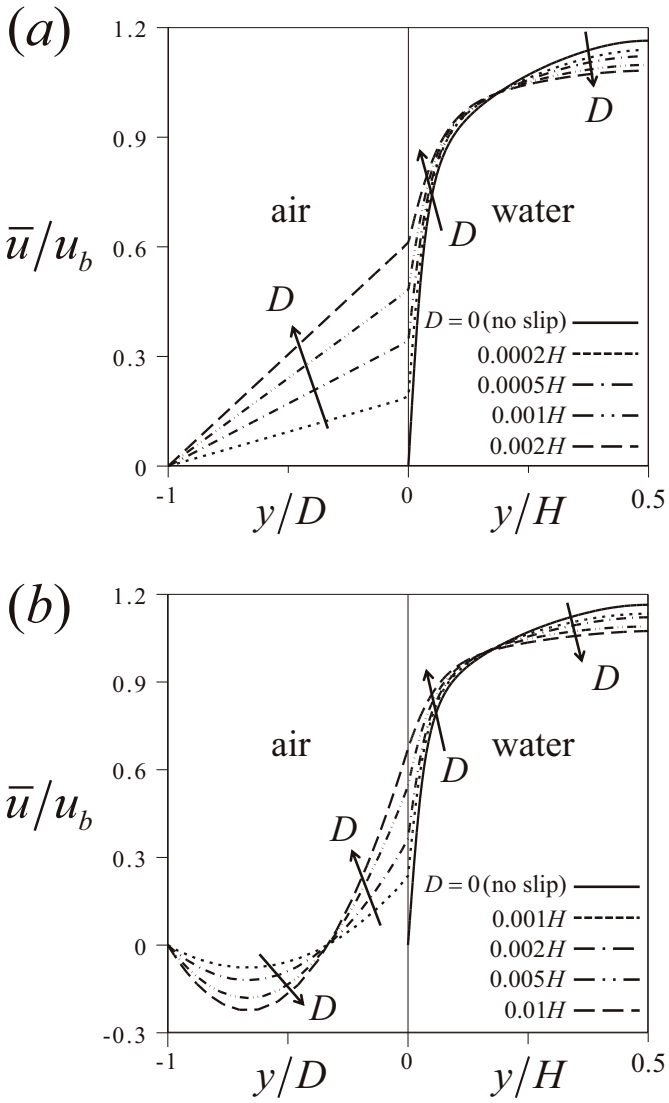

Figure 3.9. Mean velocity profiles in air and water: (a) case 1; (b) case 2.

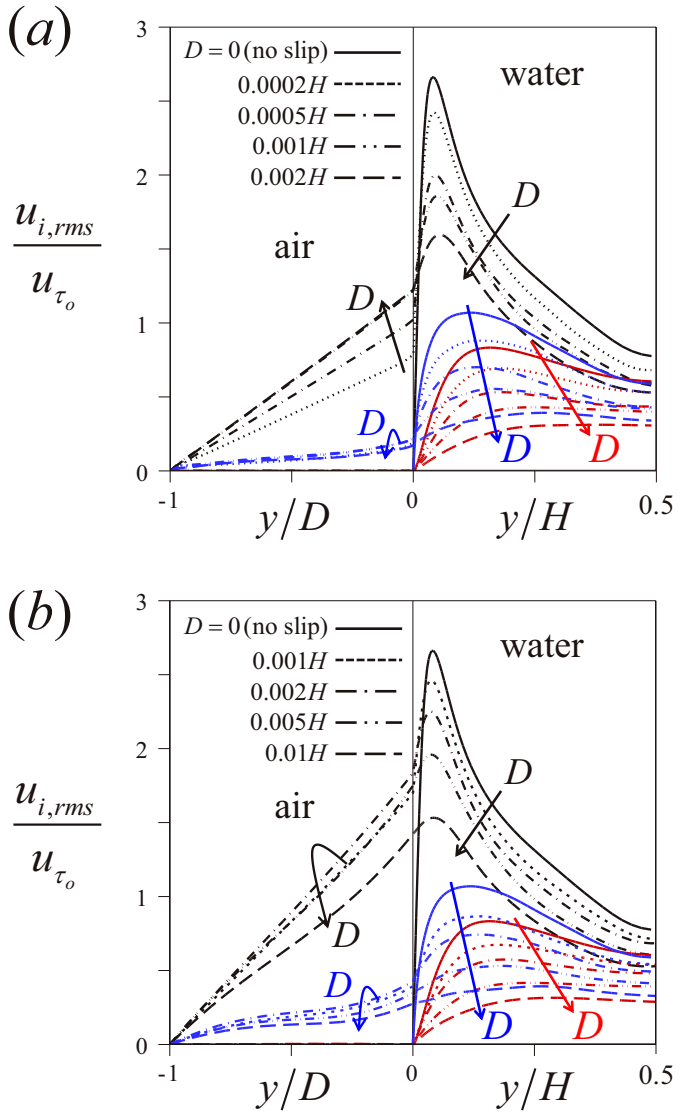

Figure 3.10. Profiles of the rms velocity fluctuations normalized by u_{τ_o}: (a) case 1; (b) case 2. Black lines, u_{rms}; red lines, v_{rms}; blue lines, w_{rms}.

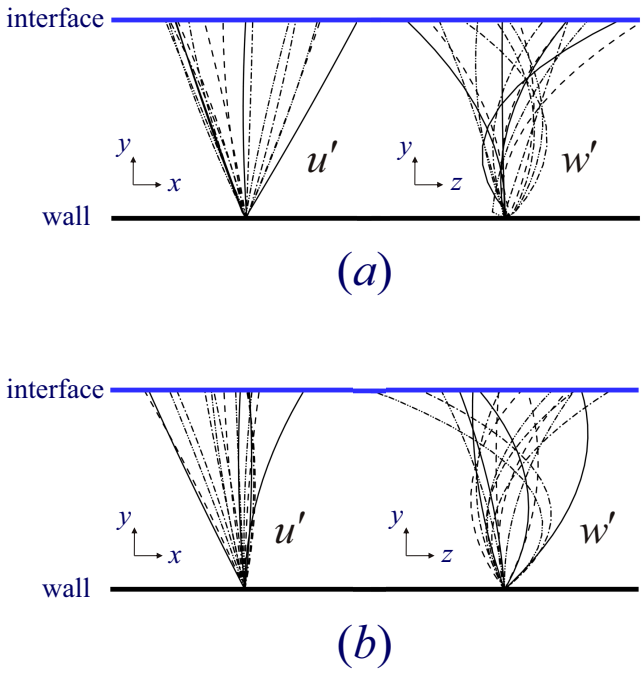

Figure 3.11. Profiles of the instantaneous velocity fluctuations (u' and w') inside the air layer at every eighth grid point: (a) case 1 ($D = 0.0005H$); (b) case 2 ($D = 0.002H$).

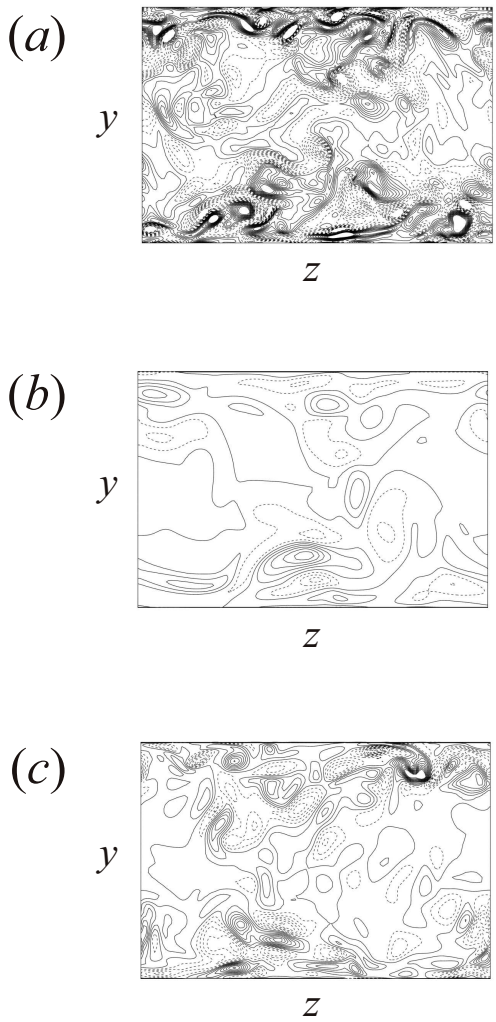

Figure 3.12. Contours of the instantaneous streamwise vorticity in a cross-flow plane for $D = 0.002H$: (a) no-slip channel ($D = 0$); (b) case 1; (c) case 2. Contours of $\omega_x H/u_b$ are from -6 to 6 by increments of 0.6.

Chapter 4

Turbulent channel flow with superhydrophobic surfaces having longitudinal groove

4.1 Introduction

In previous chapter, DNS of turbulent channel flow with an idealized SHS was performed and the important flow properties at the air-water interface were reported. However, the actual SHS device has supporting structures, such as ridges, posts or random textures. Among these configurations, many studies considered the surface with alternating grooves and ridges in the flow direction for turbulent flows (Martell, Perot & Rothstein, 2009; Daniello, Waterhouse & Rothstein, 2009; Park, Park & Kim, 2013; Park, Sun & Kim, 2014; Jelly, Jung & Zaki, 2014; Türk *et al.*, 2014; Rastegari & Akhavan, 2015). Cheng, Teo & Khoo (2009) showed that the effective slip length is the largest with SHS consisting of longitudinal grooves at $\phi \leq 0.9$ regardless of the Reynolds number, where ϕ is the gas fraction of SHS. At $Re \geq 300$, in addition, the effective slip length of SHS with longitudinal grooves is the largest irrespective of the gas fraction. Therefore, I also consider SHS consisting of longitudinal grooves.

The parametric studies of surface grating parameters in turbulent channel flow are conducted with the assumption of a rigid air-water interface. First, I investigate which grating parameter has an important influence on the effective

slip length. To this end, the pitch length, gas fraction and air-layer thickness are varied with the macro-scaled SHS. Second, the effect of SHS in a range of the actual size on the slip is investigated since there is a restriction of size because the stability of air-water interface is determined by the groove width in a reality.

4.2 Computational details

The flow geometry and coordinate system are shown in Figure 2.1 with the surface grating parameters (L_p, L_g, D). The unsteady incompressible Navier-Stokes and continuity equations are solved in both water and air, together with an immersed boundary method (Kim, Kim & Choi, 2001) to satisfy the no-slip boundary condition on the longitudinal ridges. With zero interface curvature (i.e., neglecting the surface tension effect), the wall-parallel velocities and shear stresses are matched at the air-water interface. Uniform grids are used in the streamwise and spanwise directions, while non-uniform grids are used in the wall-normal direction. The flow inside the air layer is considered as the shear-driven flow ($\Pi_g = 0$). All simulations are started from a fully developed turbulent channel flow with no-slip wall.

For performing DNS of turbulent channel flow with a macro-scaled longitudinal texture, the computational domain is the same as that of an idealized SHS: $(L_x, L_y, L_z) = (3H, H + 2D, 1.5H)$. More fine grid points are used in the spanwise direction than the case of with an idealized SHS for resolving the roughened surfaces: $(N_x, N_y, N_z) = (128, 129 + 24 \sim 64, 256)$ The air-layer thicknesses (D) are varied from $0.002H$ to $0.05H$ and the pitch length are $0.5H$, $0.75H$ and $1.5H$. The gas fractions considered are 0.25, 0.5 and 0.75 and the groove width is determined by the relationship between the pitch length and gas fraction $(L_g = L_p\phi)$.

The minimal flow unit by Jiménez & Moin (1991) is adopted for simulating micro-scaled longitudinal grooves. Choi, Moin & Kim (1993) showed the turbulence characteristics over the streamwise-aligned riblets are sustained in the minimal channel flow. The computational domain of $1.5H \times (H + 2D) \times 0.34H$ is used in the streamwise, wall-normal and spanwise directions, respec-

tively, with $16 \times (129 + 64) \times 1024$ grids. The grid spacings in wall units are $(\Delta x^{+o}, \Delta y^{+o}_{min}, \Delta z^{+o}) = (33, 0.1, 0.1)$. One configuration is only considered for micro-scale SHS: $L_p^{+o} \approx 3.8, L_g^{+o} \approx 3.3, D^{+o} \approx 18$. The groove width considered is in the range of actual SHS (Daniello, Waterhouse & Rothstein, 2009; Woolford *et al.*, 2009; Park, Sun & Kim, 2014), so the interface can be sustained with overcoming the pressure fluctuations near the interface.

4.3 Results

4.3.1 Effective slip length and skin-friction drag reduction

For a laminar flow, Lauga & Stone (2003) showed the effective slip length of the configuration with no-slip and shear-free patterns in the flow direction is a function of L_p and ϕ as

$$b_{eff} = \frac{L_p}{\pi} \ln \left[\sec \left(\frac{\pi \phi}{2} \right) \right], \tag{4.1}$$

where L_p is the pitch length and ϕ is the gas fraction. With increasing the pitch length and gas fraction, the effective slip length increase according to Eq. (4.1).

For a turbulent flow, the influence of the surface grating parameters on the effective slip length is shown in figure 4.1. The effective slip length increases with increasing gas fraction, pitch length and air layer thickness. It seems that the effective slip length is more influenced by the gas fraction than the pitch length. To further clarify a predominant parameter for the slip length, three different geometries with the same area of the air-water interface are considered. At a given groove width ($L_g^{+o} \approx 135$), Figure 4.2(a) clearly shows that the gas fraction has a more important role to the slip length than the pitch length. It is a coherent result with the theoretical relationships suggested by Lauga & Stone (2003) and Belyaev & Vinogradova (2010) for a laminar flow as shown in Fig 4.2(b). In the relationship by Belyaev & Vinogradova (2010), the local slip length b_{local} is considered as $\mu_R D$. This result is also consistent with the observation by the experiment in turbulent boundary layers ($Re_{tau} \sim 200$) (Park, Sun & Kim, 2014). The increment of air-layer thickness has also a beneficial effect on the slip length, but its effect is not crucial since the slip area is determined in the wall-parallel directions. In short, the effective slip length is

L_p	$1.5H$		$0.75H$	
ϕ	0.75	0.5	0.75	0.5
current study	0.135	0.038	0.098	0.033
Park (2015)	0.332	0.083	0.269	0.071

Table 4.1. The effective slip length normalized by H with different SHS geometries.

determined by the total amount of trapped air inside the longitudinal grooves and the gas fraction is a key parameter.

The comparison between the effective slip lengths of laminar and turbulent flows is conducted. Note that the (apparent) slip length of turbulent flow is the same as that of laminar flow in the condition of no texture on the surface (see §3.3). The effective slip length of turbulent flow is less than that of laminar flow as shown in Figure 4.3. This result can be deduced since the shear stress at the no-slip regions in turbulent flows is generally much larger than that in laminar flows. Table 4.1 shows the comparable data. The effective slip length by considering the air layer is much less than that by prescribing shear-free boundary condition at the air-water interface. This result indicates that the air-water interface should have a non-negligible shear stress.

For both laminar and turbulent flows, the DR rates estimated by the change of the mean pressure gradient for the surface grating parameters are shown in Figure 4.4. Figure 4.4(a) corresponds to three different values of gas fraction with a fixed L_p, whereas Figure 4.4(b) three distinct values of L_p with ϕ held constant at 0.5. With the growth of the total amount of trapped air inside SHS (i.e., L_p, ϕ and D increase), the DR rate also increases. The relation between the DR rate and surface grating parameters is similar to the effective slip length.

The DR rate of turbulent flow is larger than that of laminar flow. The reason is presumed as weakening of near-wall turbulence (Park, Park & Kim, 2013; Rastegari & Akhavan, 2015). As mentioned §1.3, Park, Park & Kim (2013) found that the amount of turbulent DR is well correlated with the effective slip length normalized by the viscous wall unit. This argument can be demonstrated by the log-law of Dean's formula shifted by the constant slip velocity (Dean, 1978):

$$\frac{U_c - u_s}{u_\tau} = \frac{1}{\kappa}\ln(Re_\tau) + C, \tag{4.2}$$

where U_c is the centerline velocity, κ is a Von Karman constant, and C is an empirical constant. This equation is rewritten as (see Fukagata, Kasagi & Koumoutsakos (2006) for more details)

$$b^+ = \frac{U_c}{u_{\tau_o}}\left(\frac{1}{\sqrt{1-DR}} - 1\right) - \frac{1}{\kappa}\ln(\sqrt{1-DR}). \tag{4.3}$$

Figure 4.5 shows the variation of the DR rate with the effective slip length normalized by the shear velocity at the air-water interface, u_τ, together with the results from Park (2015). As indicated by Park, Park & Kim (2013), the DR rate correlates well with the slip length in the viscous wall unit, irrespective of the surface grating parameters. Note that the effect of spanwise slip does not reflected in Eq. (4.3). From these results, I deduce that the longitudinal ridges disrupts the development of spanwise slip.

4.3.2 Spanwise variations of the flow properties at the interface

Figure 4.6 shows the normalized streamwise velocity at the interface. Note that the black and green line represent the mean slip velocity ($\bar{u}_s/u_b$) averaged in time and wall-parallel directions and the slip velocity (u_s/u_b) averaged in time

and the streamwise direction, respectively. From Figure 4.6(a), as ϕ increase with a fixed L_p, the magnitude of streamwise velocity at the air-water interface increases. The slip velocity varies in the spanwise direction and its maximum value is yielded near the center region of groove. Referring to Figure 4.6(b), it is shown that the slip velocity increases with the growth of pitch length. These trends have a good agreement with the results of Maynes *et al.* (2007) and Teo & Khoo (2009) in laminar flow. The upper limit of normalized slip velocity is one where the slip velocity is the same as the bulk velocity (as known as a plug flow). The mean slip velocity has a distance to the upper limit, whereas the local slip velocity approaches to the value of one as ϕ increases. This is because the groove widths are too broad $L_g^{+o} \approx 90 \sim 270$.

The dependence of the skin friction coefficient on the surface geometry is presented in Figure 4.7. The skin friction coefficient, which means the ratio of shear stress at the interface (τ_s) to dynamic pressure, is defined as $C_f = \tau_s/(\rho_l u_b^2/2)$. With increasing ϕ and L_p, the skin-friction coefficient decreases. The peak values of C_f are observed at the edges of ridge. C_f on the ridge surface are similar to $C_{f,noslip}$, whereas the friction drags almost vanish at the air-water interface, indicating the shear-free interface. As shown in Figure 4.7(c) and (d), however, $C_{f,max}$ is almost 1/3 $C_{f,noslip}$ where $D = 0.002H$. It has very large the aspect ratio, where the aspect ratio is defined as the groove width of air-layer thickness. The effect of aspect ratio has also to be investigated later.

Figure 4.8 shows the slip length for the streamwise velocity and velocity gradient at the interface. As ϕ and L_p increase, the slip length slightly increases. With large grooves, the local slip length at the air-water interface is almost reached at the apparent slip length ($b_{app} = \mu_R D$). It implies that the velocity profiles near the core regions are near plug flow, since the slip velocity is almost 90% of bulk velocity. So turbulent intensities may be almost vanished. Figure

4.9 shows the scatter plots with four distinct locations in the spanwise direction. This result is very impressive that the new slip model proposed in Chapter 3 is valid with the SHS consisting of longitudinal grooves. As shown in Figure 4.9, the local spanwise slip length (b_z) is a quarter of the value of the local streamwise slip length (b_x) and thus this result is consistent with our new slip model ($b_z = 1/4b_x$). By prescribing shear-free boundary condition at the air-water interface, the local spanwise slip length is an infinity. Therefore, this result is very important to announce the flow properties at the interface.

Figure 4.10 shows near-wall turbulence structures. As shown in figure, near-wall vortical structures disappear, resulting in smaller skin-friction drag. This demonstrates that there is a strong correlation between the strength of near-wall streamwise vortices.

4.4 Microrgates: an actual device size

There is a restriction of size because the stability of air-water interface is determined by the groove width ($L_g = L_p\phi$). Türk *et al.* (2014) reported that the proper groove size $L_g^{+o} \ll 300$ with an actual flow condition of ocean transports where $u_\tau \sim 0.5m/s$ and the pressure fluctuation on the surface is an order of one. The groove widths considered with the macro-scaled SHS are nearly 50 to 400 in the viscous wall units, so the extended investigation of flow characteristics over the micro-scaled SHS is clearly required

The actual size of the groove width and pitch length is an order of one (Daniello, Waterhouse & Rothstein, 2009; Woolford *et al.*, 2009; Park, Sun & Kim, 2014). For resolving the micro-scaled ridges, more fine grid points are needed in the spanwise direction, so the computational cost required is too expensive. The approach in the present study is based on the work of Jiménez & Moin (1991), which demonstrated that the essential dynamics associated with the streamwise vortical structures present in the wall region can be reproduced in what they referred to as the "minimal channel" flow (Choi, Moin & Kim, 1994). Of course, some structures are absent in the minimal channel flow. However, since the near-wall turbulence statistics were reproduced accurately, Jiménez & Moin (1991) implied that such interactions may not be essential to turbulence dynamics in the wall region. Choi, Moin & Kim (1993) adopted the minimal channel flow for DNS of turbulent channel flow over the streamwise-aligned riblets and successfully showed the turbulence characteristics. In the present study, the computational domain and grid points are the same as the data of Choi, Moin & Kim (1993) except in the spanwise direction. More grid points are required in the spanwise direction for resolving micro-textures ($\sim O(1)$).

Figure 4.11 shows the the time history of the average pressure gradient inside the water region. The overlap regions of pressure gradient with no-slip wall and that with SHS intermittently exist and the frequency is lower than that with a regular domain size. To observe a clear trend of the pressure gradient, time-averaging is conducted. The history of plane- and time-averaged pressure gradient, i.e. $1/t \int_0^t \Pi_l^*(\tau) d\tau$ are also shown in figure 4.11. The skin-friction reduction by the SHS is clearly shown and the percentage of DR rate is near 13%. The present DR rate is much less than that of experimental data (maximum DR $\sim$ 50% and 75%) using similar SHS geometries (Daniello, Waterhouse & Rothstein, 2009; Park, Sun & Kim, 2014). Computational grid and domain size test is required rigorously.

Figure 4.12 shows the mean velocity profiles and the modified mean velocity profiles. In Figure 4.12(a), there is an upward shift by the slip velocity $\bar{u}_s^+ \approx 1.7$. Min & Kim (2004) reported that modified mean velocities fall on one curve for b_x only, but show downward shifts for combined b_x and b_z, indicating that the present interface has non-trivial b_z. Figure 4.13 shows the rms velocity fluctuations. Due the slip velocities at the interface, the u_{rms} and w_{rms} are non-zero value at the interface. Figure 4.14 shows the contours of velocity component with the pattern-averaging. As shown in Figure 4.14, the pattern-averaged streamwise velocity and rms velocity fluctuations have monotonous variations in the spanwise and wall-normal directions. Thus, there is no significant variation in the spanwise and wall-normal directions. However, v_{rms} indicates that the flow properties at the interface should be varied in the spanwise direction. Figure 4.15 shows the variations of patterned-averaged slip velocity and slip length in the spanwise direction. The maximum slip velocity is near $0.15u_b$, so the velocity near the core regions of groove still remains the parabola, unlike the case with macro-SHS which has the plug flow near the groove-center regions.

In Figure 4.15(c), the maximum slip length is approximately $0.2H$, whereas the macro-SHS has the apparent slip length at the center region. With the surface parameters of micrograte, the apparent slip length is determined at $2.8H$. Since the small pitch length is accompanied by small groove width, the growth of the slip velocity and slip length at the air-water interface is inhibited. The effective slip length of SHS with micrograte is an order of the viscous sublayer thickness, so the drag reduction rate was less than 20%.

4.5 Summaries

In this chapter, longitudinal grooves and ridges were considered as the surface roughness of SHS and DNSs for investigating the effect of surface geometry were performed. The grating parameters of SHS considered were the air-layer thickness, pitch length and groove width (or gas fraction). A wide range of texture sizes were simulated from microscale $O(1)$ to macroscale $O(10^2)$ in the viscous wall unit. For both micro- and macro-scaled SHSs, the surface grating parameters had profound effects on the skin-friction drag, slip velocity and effective slip length. Among the surface grating parameters, the gas fraction played a more important role for the slip than the pitch length and air-layer thickness. With the larger pitch length relative to the channel height, the drag reduction rate approached to the gas fraction, indicating that the shear stress at the air-water interface is almost vanished. However, the non-negligible shear stress remained at the interface when the groove is not broad. This result suggested that SHSs should have a large groove width to obtain the high drag reduction. However, the actual devices have a micron size for the groove since the interface rigidity decreases as the groove width increases. For resolving the small pitch length and groove width, the minimal flow unit was adopted. The effective slip length was an order of the viscous sublayer thickness, so the drag reduction rate was less than 20%. The amount of drag reduction can be estimated by the effective slip length normalized by the viscous wall unit regardless of the geometry.

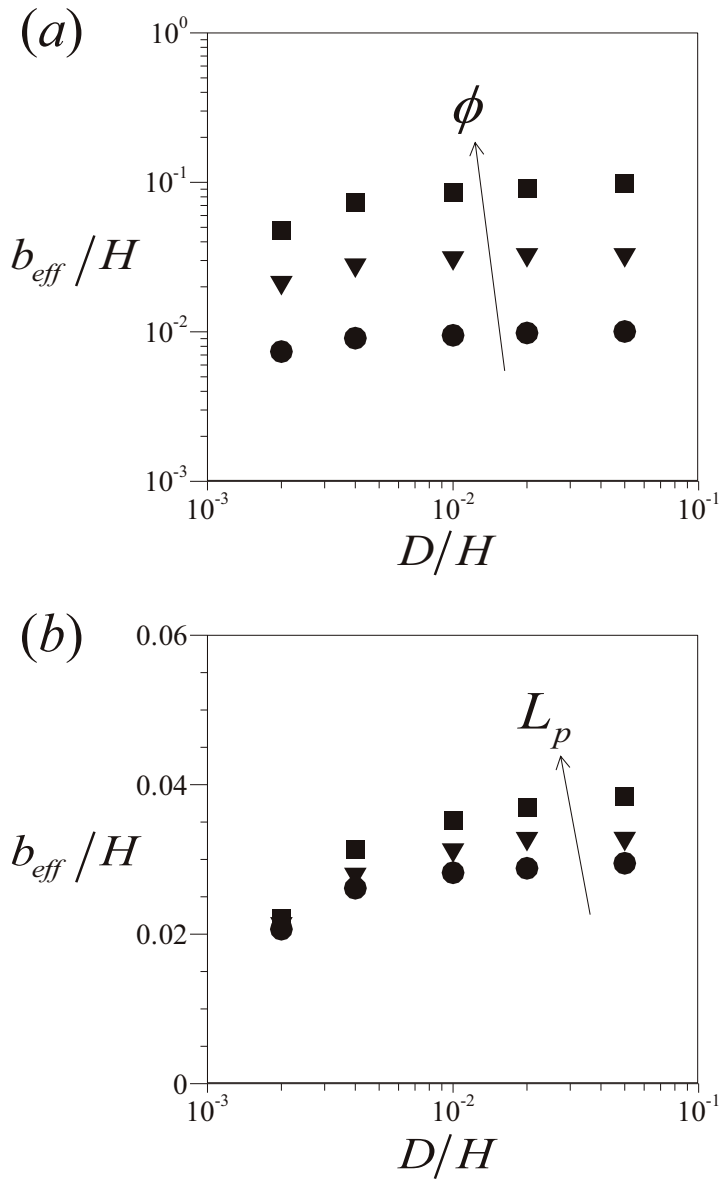

Figure 4.1. Variation of the effective slip length with different SHS geometry: (a) $L_p = 0.75H$; (b) $\phi = 0.5$. Symbols denote the gas fraction (square, $\phi = 0.75$; gradient, $\phi = 0.5$; circle, $\phi = 0.25$).

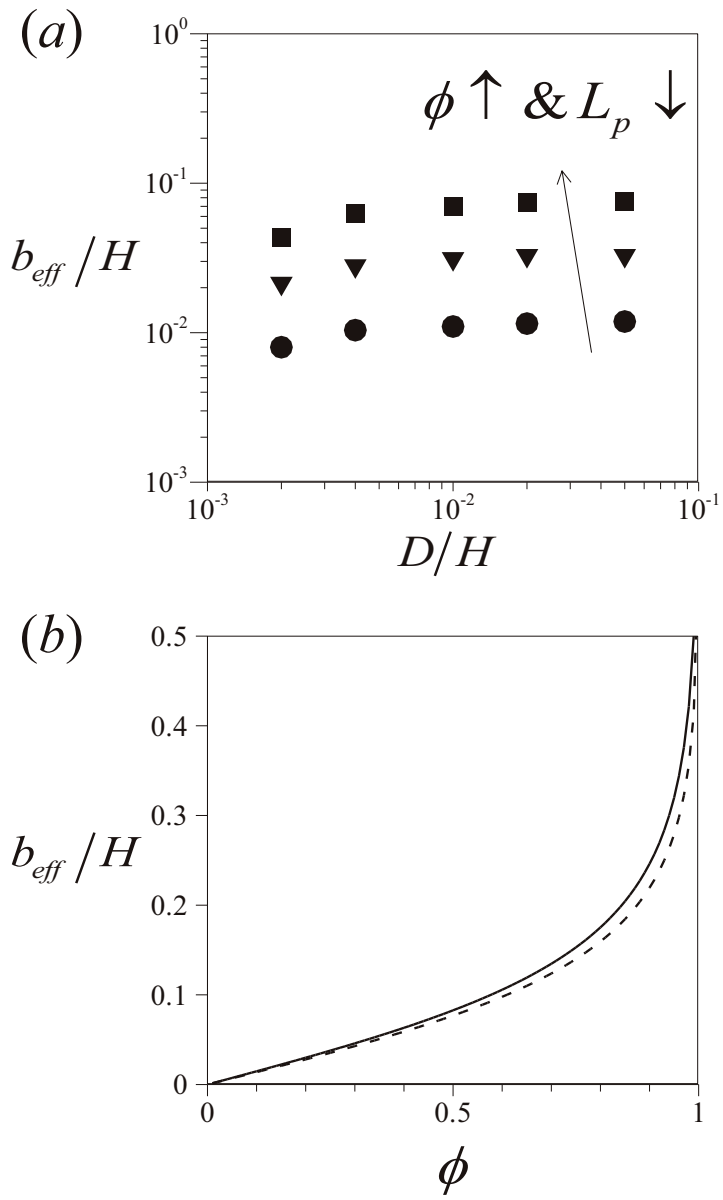

Figure 4.2. Variation of the effective slip length for a groove width $L_g = 0.375H$: (a) turbulent flow; (b) laminar flow. In (a), symbols denote the gas fraction (square, $\phi = 0.75$; gradient, $\phi = 0.5$; circle, $\phi = 0.25$). In (b), the results are calculated by Eqs. (4.1) and (2.32) with an assumption of $D = \infty$ and $D = 0.05H$, respectively.

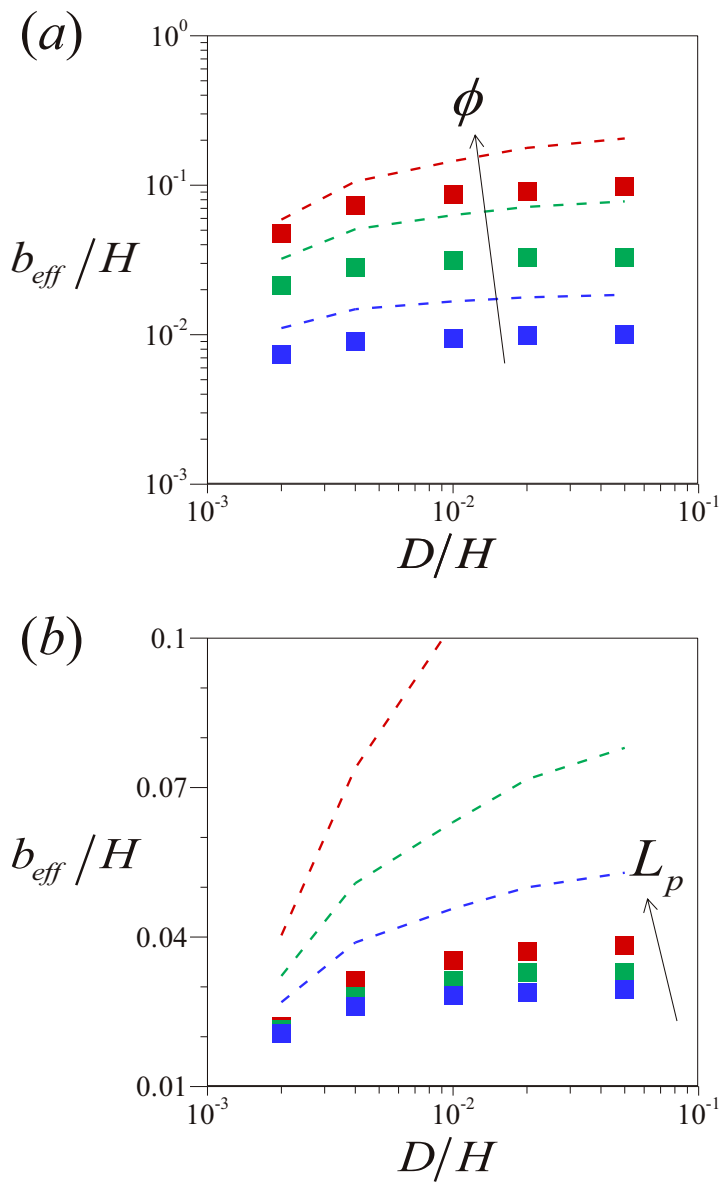

Figure 4.3. Variation of the effective slip length with different SHS geometry: (a) $L_p = 0.75H$; (b) $\phi = 0.5$. Symbol denotes the result of turbulent flow and dashed line denotes the result of laminar flow. In (a), colors denote the gas fraction (red, $\phi = 0.75$; green, $\phi = 0.5$; blue, $\phi = 0.25$). In (b), colors denote the pitch length (red, $L_p = 1.5H$; green, $L_p = 0.75H$; blue, $L_p = 0.5H$).

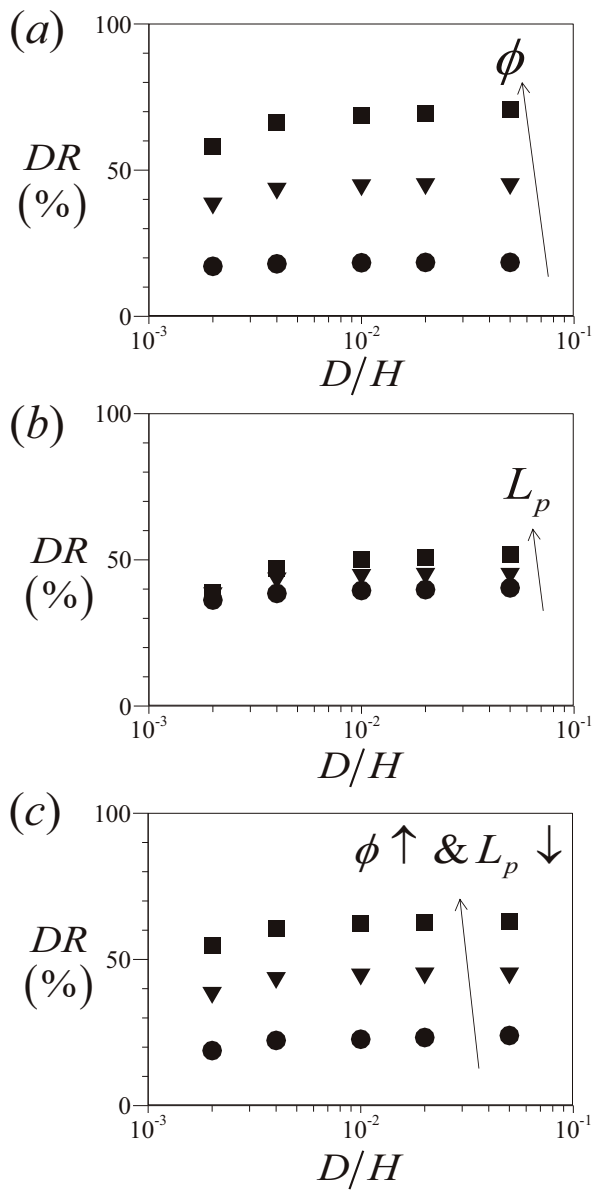

Figure 4.4. Variation of the DR rate with the surface grating parameters: (a) $L_p = 0.75H$; (b) $\phi = 0.5$ (c) $L_g = 0.375H$. Symbols represent the gas fraction (square, $\phi = 0.75$; gradient, $\phi = 0.5$; circle, $\phi = 0.25$).

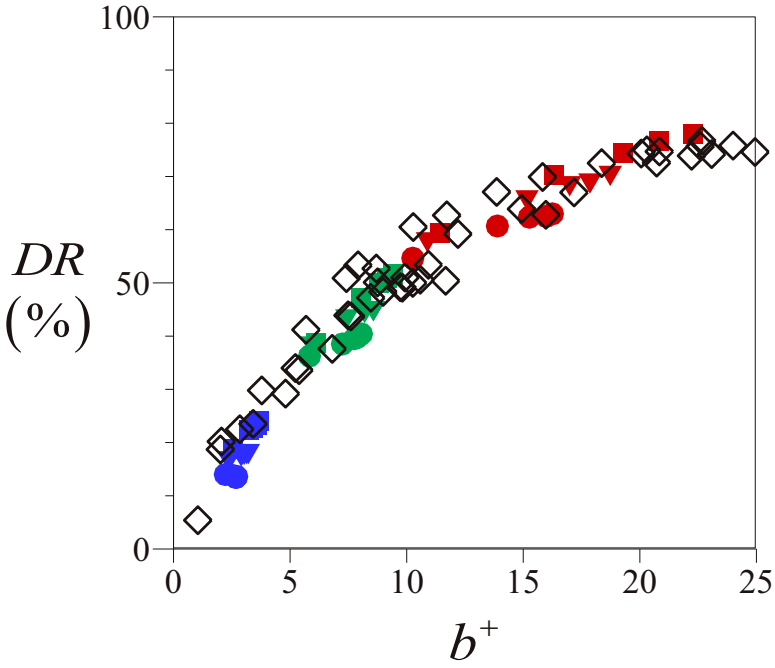

Figure 4.5. Variations of the DR rate with the effective slip length in wall units. Colored symbols represent the gas fraction (square, $\phi = 0.75$; gradient, $\phi = 0.5$; circle, $\phi = 0.25$), and colors denote the pitch length (red, $L_p = 1.5H$; green, $L_p = 0.75H$; blue, $L_p = 0.5H$). Open diamonds are the DNS results from various SHS geometry and Reynolds number (Park, 2015).

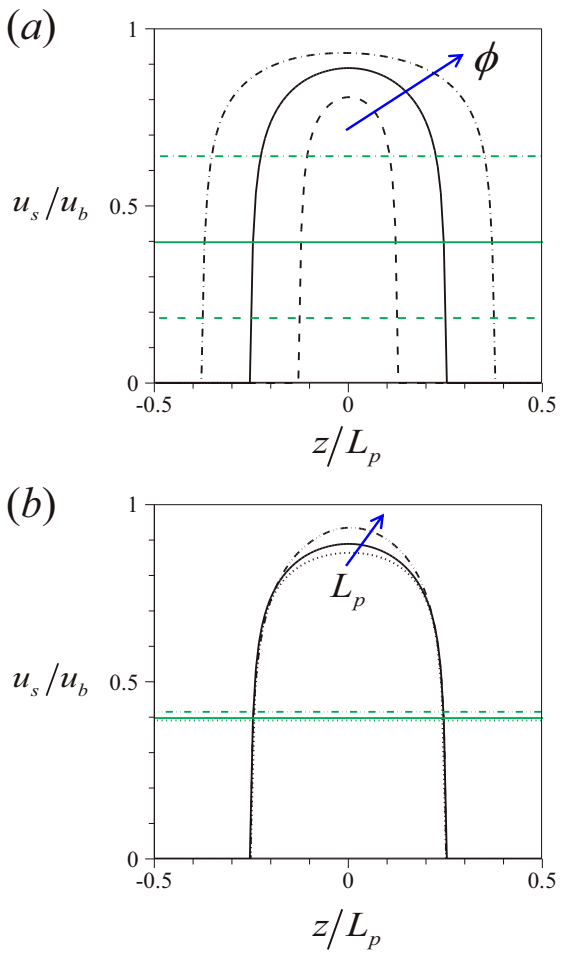

Figure 4.6. Distribution of time-averaged streamwise velocity at the interface with constant $D = 0.05H$: (a) various gas fractions $\phi = 0.25, 0.5$, and 0.75 with $L_p = 0.75H$; (b) various pitch lengths $L_p = 0.5H, 0.75H$, and $1.5H$ with $\phi = 0.5$. The green lines denote the mean properties.

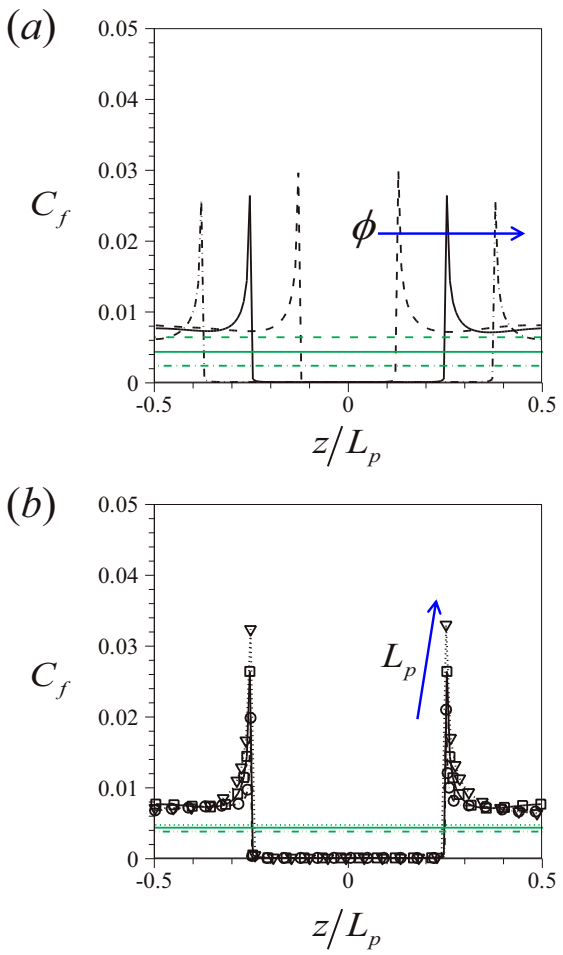

Figure 4.7. For caption see the following page.

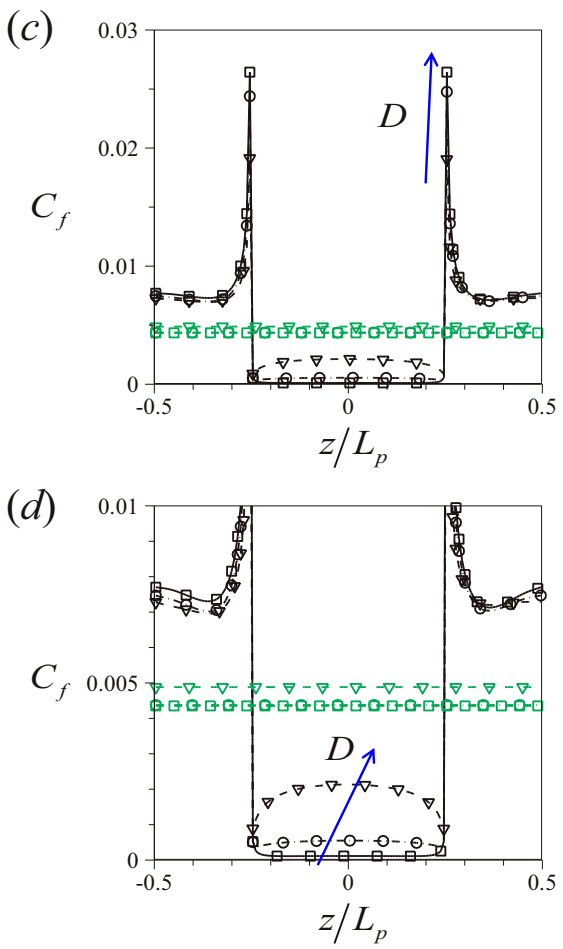

Figure 4.7. Distribution of time-averaged skin-friction coefficient at the interface with constant $D = 0.05H$: (a) various gas fractions $\phi = 0.25, 0.5$, and 0.75 with Ł$_p = 0.75H$; (b) various pitch lengths $L_p = 0.5H, 0.75H$, and $1.5H$ with $\phi = 0.5$. (c) various gas fractions $\phi = 0.25, 0.5$, and 0.75 with Ł$_p = 0.75H$; (d) various pitch lengths $L_p = 0.5H, 0.75H$, and $1.5H$ with $\phi = 0.5$. Gradient, square and circle, respectively, denote Ł$_p = 0.5H, 0.75H$, and $1.5H$. The green lines denote the mean properties.

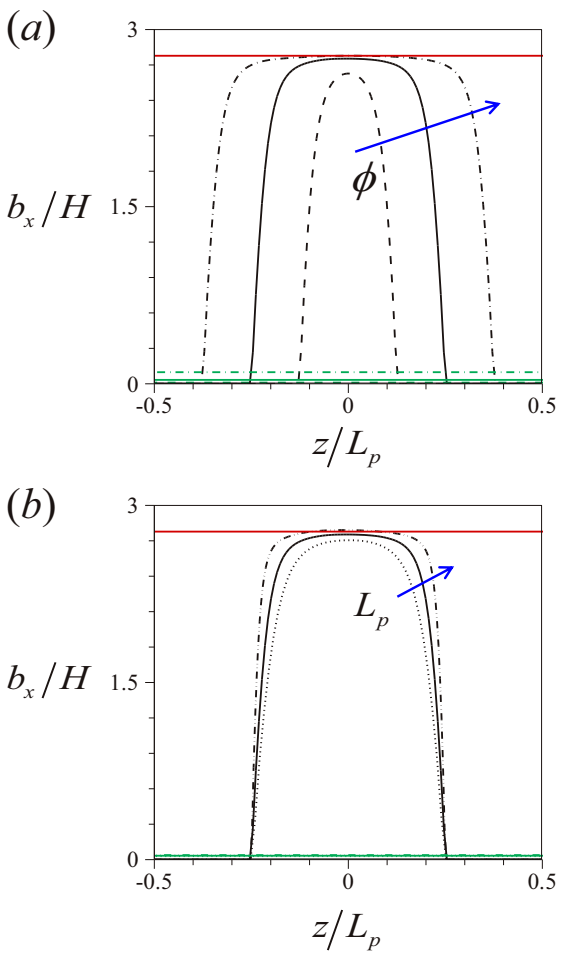

Figure 4.8. Distribution of time-averaged local slip length from the streamwise velocity components at the interface with constant $D = 0.05H$: (a) various gas fractions $\phi = 0.25, 0.5$, and 0.75 with $L_p = 0.75H$; (b) various pitch lengths $L_p = 0.5H, 0.75H$, and $1.5H$ with $\phi = 0.5$. The green and red lines denote the mean properties and the case of $\phi = 1.0$, respectively.

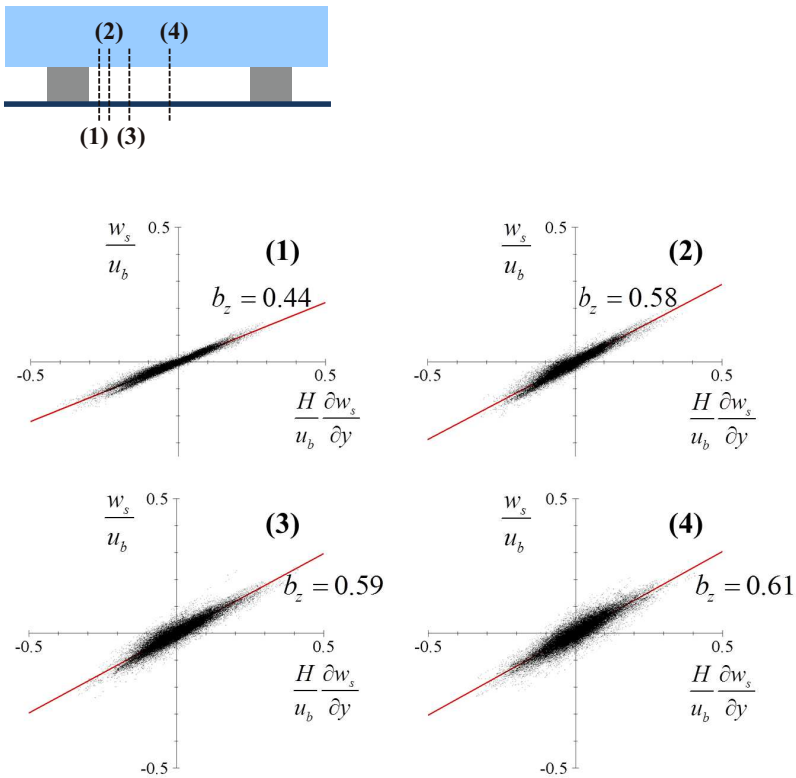

Figure 4.9. Scatter plot of local slip velocity vs velocity gradient at the interface at the four different location in the spanwise direction at $L_p = 0.75H$, $\phi = 0.5$ and $D = 0.05H$. The number of plot represents the location.

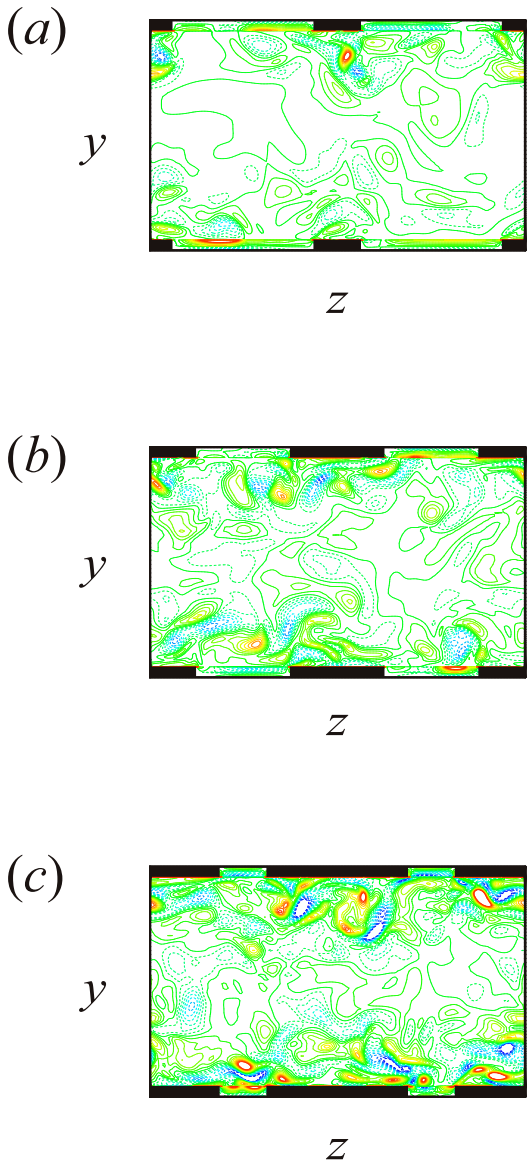

Figure 4.10. Contours of the instantaneous streamwise vorticity in a cross-flow plane for $L_p = 0.75H$ and $D = 0.05H$: (a) $\phi = 0.25$; (b) $\phi = 0.5$; (c) $\phi = 0.75$. Contours of $\omega_x H/u_b$ are from -6 to 6 by increments of 0.6.

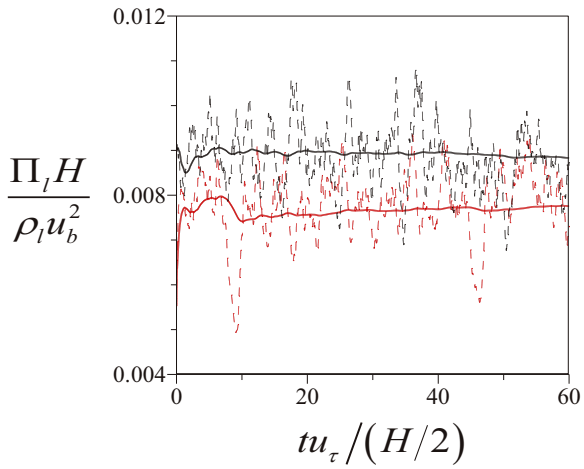

Figure 4.11. Time history of pressure gradient in the water region: black, with no-slip wall; red, with SHS. The solid lines denote time-averaged pressure gradients.

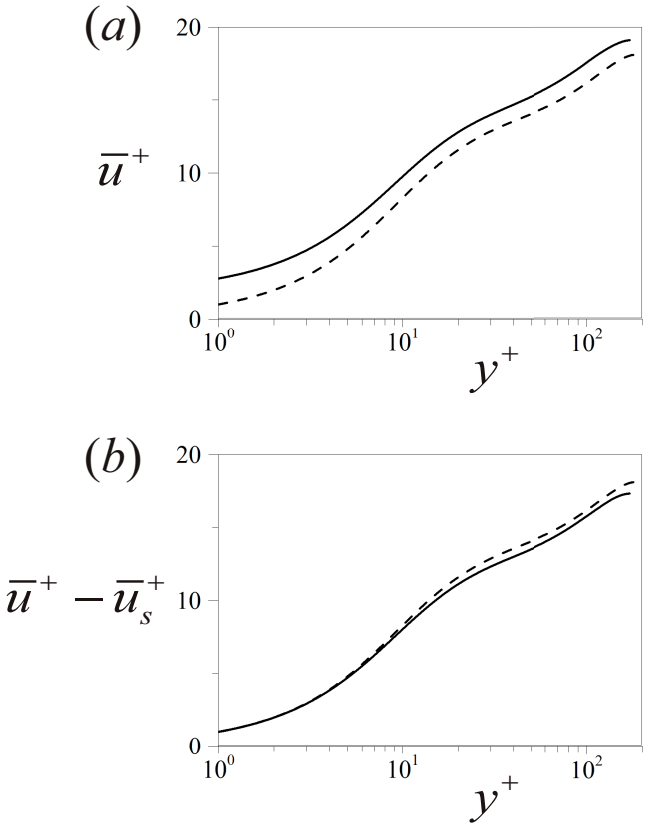

Figure 4.12. (a) Mean velocity profiles in wall units; (b) modified velocity profiles with the slip velocity substracted.

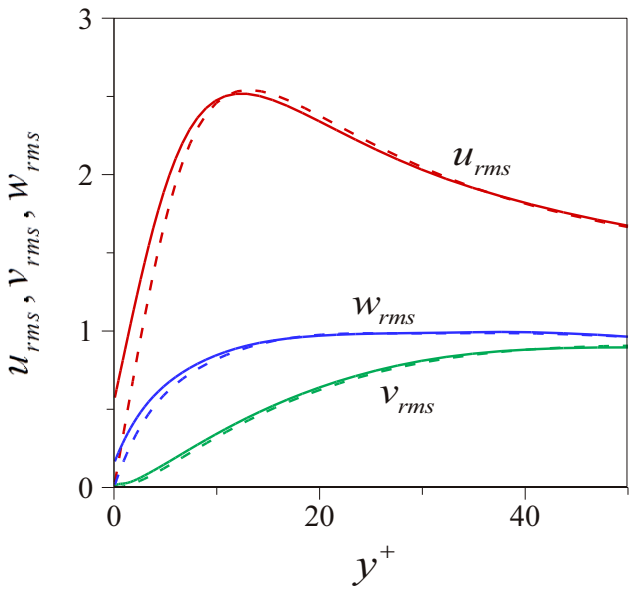

Figure 4.13. Profiles of the rms velocity fluctuations normalized by u_{τ_o}: solid, result with no-slip wall; dashed, result with SHS.

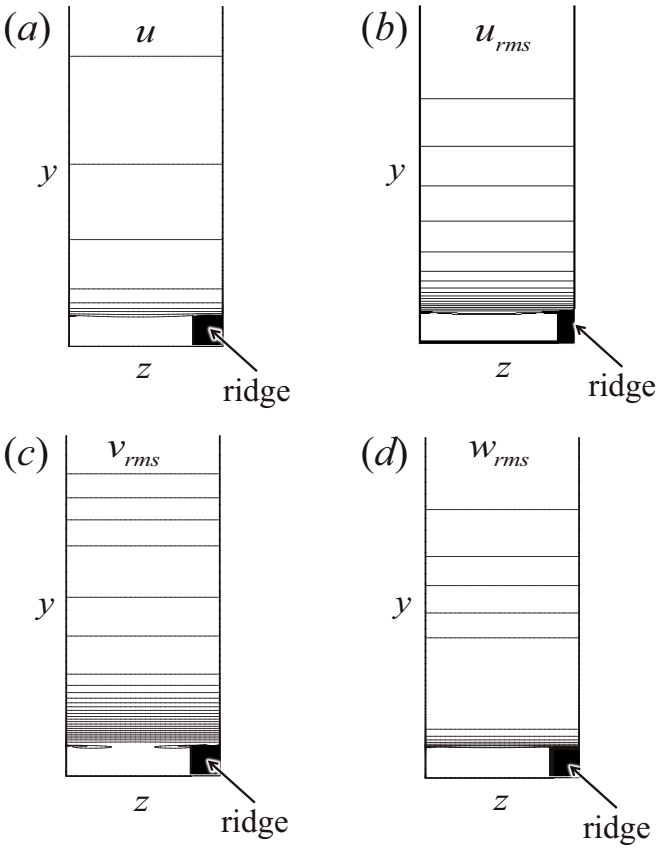

Figure 4.14. Contours of the velocity components with micrograts: (a) streamwise velocity; (b) u_{rms}; (c) v_{rms}; (d) w_{rms}. The plot domain extends from the lower SHS to the centerline of the channel.

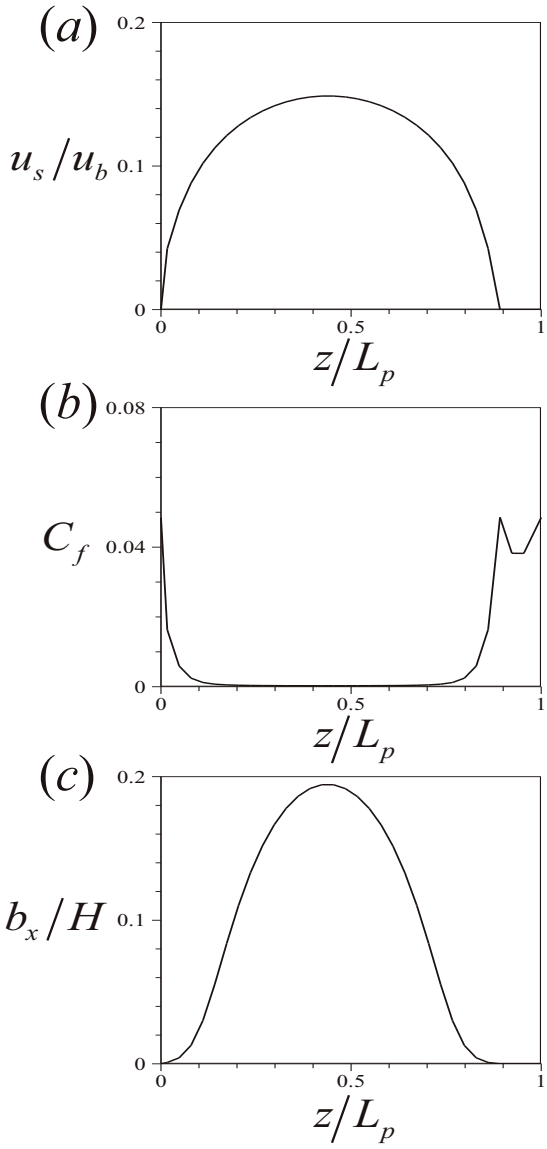

Figure 4.15. Spanwise variations of flow properties at the interface: (a) slip velocity; (b) skin-friction coeffiient; (c) slip length.

Chapter 5

Summary and Concluding Remarks

In the present study, I investigated the effects of SHSs on the slip length and skin-friction reduction. For this purpose, the flow inside the air layer underneath the water turbulent flow was directly simulated with the assumption that the interface was flat (neglecting the surface tension effect). Two different kinds of SHS were considered: an idealized SHS without supporting structures and SHS with longitudinal grooves.

For an ideal case, two different flow types inside the air layer were considered: a shear-driven flow and a recirculating flow with zero net mass flow rate. The slip length, slip velocity and drag reduction rate increased as the air-layer thickness increased. At a given air-layer thickness, the shear-driven flow in the air layer supplied more slip than the recirculating flow. However, when the slip length was the same, there seemed no clear difference in the drag reduction rate and slip velocity between two cases. The present drag reduction rate fell in between those from the streamwise slip only and isotropic slip, indicating that the present air-water interface generates an anisotropic slip (stronger in the streamwise slip than in the spanwise one). It is shown that the Navier slip model should be applied to mean values only, and not to instantaneous (or fluctuating) quantities. In this regard, I proposed a new slip model that provides more slip in the streamwise direction than in the spanwise direction.

For a textured case, a wide range of sizes were explored from $O(1)$ to $O(10^2)$

in the viscous wall unit. The slip properties, such as the slip length, slip velocity and drag reduction rate, increased as the grating parameters increased. The gas fraction played a key role for the slip properties with a large pitch length. As the pitch length and air-layer thickness increased, the drag reduction rate approached to the gas fraction, indicating that the shear stress at the air-water interface is almost vanished. These results suggested that SHSs should be manufactured with a large groove width to obtain the high drag reduction. However, the actual devices have a micron size for the groove since the interface rigidity decreases as the groove width increases. For resolving the small pitch length and groove width, the minimal flow unit was adopted. The effective slip length was an order of the viscous sublayer thickness, so the drag reduction rate was less than 20%.

The air-water interface is assumed to be flat in this study. In reality, however, the interface is sustained by the surface tension from the edges of SHS texture, and is curved and moves owing to air dissolution and turbulent pressure fluctuations. This important subject is to be investigated in the near future.

References

Aljallis, E., Sarshar, M. A., Datla, R., Sikka, V., Jones, A. & Choi, C.-H. 2013 Experimental study of skin friction drag reduction on superhydrophobic flat plates in high reynolds number boundary layer flow. *Phys. Fluids* **25**, 025103.

Bech, K. H., Tillmark, N., Alfredsson, P. H. & Andersson, H. I. 1995 An investigation of turbulent plane Couette flow at low Reynolds numbers. *J. Fluid Mech.* **286**, 291–325.

Belyaev, A. V. & Vinogradova, O. I. 2010 Effective slip in pressure-driven flow past super-hydrophobic stripes. *J. Fluid Mech.* **652**, 489–499.

Busse, A. & Sandham, N. D. 2012 Influence of an anisotropic slip-length boundary condition on turbulent channel flow. *Phys. Fluids* **24**, 055111.

Busse, A., Sandham, N. D., McHale, G. & Newton, M. I. 2013 Change in drag, apparent slip and optimum air layer thickness for laminar flow over an idealised superhydrophobic surface. *J. Fluid Mech.* **727**, 488–508.

Ceccio, S. L. 2010 Friction drag reduction of external flows with bubble and gas injection. *Annu. Rev. Fluid Mech.* **42**, 183–203.

Cheng, Y. P., Teo, C. J. & Khoo, B. C. 2009 Microchannel flows with superhydrophobic surfaces: Effects of Reynolds number and pattern width to channel height ratio. *Phys. Fluids* **21**, 122004.

Choi, C.-H., Johan, K., Westin, A. & Breuer, K. S. 2003 Apparent slip flows in hydrophilic and hydrophobic microchannels. *Phys. Fluids* **15**, 2897.

Choi, C.-H., Ulmanella, U., Kim, J., Ho, C.-M. & Kim, C.-J. 2006

Effective slip and friction reduction in nanograted superhydrophobic microchannels. *Phys. Fluids* **18**, 087105.

Choi, H., Moin, P. & Kim, J. 1991 On the effect of riblets in fully developed laminar channel flows. *Phys. Fluids A* **3**, 1892–1896.

Choi, H., Moin, P. & Kim, J. 1993 Direct numerical simulation of turbulent flow over riblets. *J. Fluid Mech.* **255**, 503–539.

Choi, H., Moin, P. & Kim, J. 1994 Active turbulence control for drag reduction in wall-bounded flows. *J. Fluid Mech.* **262**, 75–110.

Cottin-Bizonne, C., Barentin, C., Charlaix, E., Bocquet, L. & Barrat, J. L. 2004 Dynamics of simple liquids at heterogeneous surfaces: Molecular-dynamics simulations and hydrodynamic description. *Eur. Phys. J. E.* **15**, 427–438.

Daniello, R. J., Waterhouse, N. E. & Rothstein, J. P. 2009 Drag reduction in turbulent flows over superhydrophobic surfaces. *Phys. Fluids* **21**, 085103.

Davies, J., Maynes, D., Webb, B. W. & Woolford, B. 2006 Laminar flow in a microchannel with superhydrophobic walls exhibiting transverse ribs. *Phys. Fluids* **18**, 087110.

Dean, R. B. 1978 Reynolds number dependence of skin friction and other bulk flow variables in two-dimensional rectangular duct flow. *ASME Trans. J. Fluids Eng.* **100**, 215.

Elbing, B. R., Winkel, E. S., Lay, K. A., Ceccio, S. L., Dowling, D. R. & Perlin, M. 2008 Bubble-induced skin-friction drag reduction and the abrupt transition to air-layer drag reduction. *J. Fluid Mech.* **612**, 201–223.

Fukagata, K., Kasagi, N. & Koumoutsakos, P. 2006 A theoretical pre-

diction of friction drag reduction in turbulent flow by superhydrophobic surfaces. *Phys. Fluids* **18**, 051703.

Goldstein, S. & Council, A. R. 1965 Modern developments in fluid dynamics. *Dover, New York*

Govindarajan, R. & Sahu, K. C. 2014 Instabilities in viscosity-stratified flow. *Annu. Rev. Fluid Mech.* **46**, 331–353.

Hahn, S. 2002 Cavity as a new passive device for reduction of skin friction and heat transfer. PhD thesis, Seoul National University.

Hahn, S., Je, J. & Choi, H. 2002 Direct numerical simulation of turbulent channel flow with permeable walls. *J. Fluid Mech.* **450**, 259–285.

Jelly, T. O., Jung, S. Y. & Zaki, T. A. 2014 Turbulence and skin friction modification in channel flow with streamwise-aligned superhydrophobic surface texture. *Phys. Fluids* **26**, 095102.

Jiménez, J. & Moin, P. 1991 The minimal flow unit in near-wall turbulence. *J. Fluid Mech.* **225**, 213–240.

Joseph, D. D. 1980 Boundary conditions for thin lubrication layers. *Phys. Fluids* **23**, 2356.

Jung, Y. C. & Bhushan, B. 2010 Biomimetic structures for fluid drag reduction in laminar and turbulent flows. *J. Phys.: Condens. Matter* **22**, 035104.

Jung, T., Choi, H. & Kim, J. 2016 Effects of the air layer of an idealized superhydrophobic surface on the slip length and skin-friction drag *J. Fluid Mech. Accepted*.

Kang, S. & Choi, H. 2000 Active wall motions for skin-friction drag reduction. *Phys. Fluids* **26**, 095102.

Kim, J., Moin, P. & Moser, H. 1987 An immersed-boundary finite-volume

method for simulations of flow in complex geometries. *J. Comput. Phys.* **171**, 132–150.

Kim, J., Kim, D. & Choi, H. 2001 An immersed-boundary finite-volume method for simulations of flow in complex geometries. *J. Comput. Phys.* **171**, 132–150.

Kim, E. & Choi, H. 2015 Spacetime characteristics of a compliant wall in a turbulent channel flow. *J. Fluid Mech.* **756**, 30–53.

Lamb, Sir H. 1916 Hydrodynamics (4th edition). Cambridge University Press, 611–612.

Lauga, E. & Stone, H. A. 2003 Effective slip in pressure-driven Stokes flow. *J. Fluid Mech.* **489**, 55–77.

Lauga, E., Brenner, M. & Stone, H. A. 2007 Microfluidics: the no-slip boundary condition. *J. Fluid Mech.* **489**, 1219–1240.

Lee, C., Choi, C.-H. & Kim, C.-J. 2008 Structured surfaces for a giant liquid slip. *Phys. Rev. Lett.* **101**, 064501.

Lee, C. & Kim, C.-J. 2009 Maximizing the giant liquid slip on superhydrophobic microstructures by nanostructuring their sidewalls. *Langmuir* **25**, 12812.

Martell, M. B., Perot, J. B. & Rothstein, J. P. 2009 Direct numerical simulations of turbulent flows over superhydrophobic surfaces. *J. Fluid Mech.* **620**, 31–41.

Maynes, D., Jeffs, K., Woolford, B. & Webb, B. W. 2007 Laminar flow in a microchannel with hydrophobic surface patterned microribs oriented parallel to the flow direction. *Phys. Fluids* **19**, 093603.

Min, T., Yoo, J. Y., Choi, H. & Joseph, D. D. 2003 Drag reduction by polymer additives in a turbulent channel flow. *J. Fluid Mech.* **486**, 213–238.

Min, T. & Kim, J. 2004 Effects of hydrophobic surface on skin-friction drag. *Phys. Fluids* **16**, L55.

Náraigh, L. Ó. & Spelt, P. D. 2010 Interfacial instability of turbulent two-phase stratified flow: Pressure-driven flow and non-Newtonian layers. *J. Non-Newtonian Fluid Mech.* **165**, 489–508.

Navier, C. 1823 Mémoire sur les dois du mouvement des fluides. *Mem. Acad. Sci. Inst. Fr.* **6**, 389–440.

Park, H., Park, H. & Kim, J. 2013 A numerical study of the effects of superhydrophobic surface on skin-friction drag in turbulent channel flow. *Phys. Fluids* **25**, 110815.

Park, H., Sun, G. & Kim, C.-J. 2014 Superhydrophobic turbulent drag reduction as a function of surface grating parameters. *J. Fluid Mech.* **747**, 722–734.

Park, H. 2015 A numerical study of the effects of superhydrophobic surfaces on skin-friction drag reduction in wall-bounded shear flows. PhD thesis, University of California, Los Angeles.

Peguero, C. & Breuer, K. 2009 On drag reduction in turbulent channel flow over superhydrophobic surfaces. *Advance in Turbulence XII*, 233–236.

Philip, J. R. 1972 Flows satisfying mixed no-slip and no-shear conditions. *J. Appl. Math. Phys.* **23**, 353–372.

Philip, J. R. 1972 Integral properties of flows satisfying mixed no-slip and no-shear conditions. *J. Appl. Math. Phys.* **23**, 960–968.

Piao, L. & Park, H. 2015 Two-dimensional analysis of air-water interface on superhydrophobic grooves under fluctuating water pressure. *Langmuir* **31**, 8022–8032.

Rastegari, A. & Akhavan, R. 2015 On the mechanism of turbulent drag reduction with super-hydrophobic surfaces. *J. Fluid Mech.* **773**, R4.

Rothstein, J. P. 2010 Slip on superhydrophobic surfaces. *Annu. Rev. Fluid Mech.* **42**, 89–109.

Seo, J., García-Mayoral, R. & Mani, A. 2015 Pressure fluctuations and interfacial robustness in turbulent flows over superhydrophobic surfaces. *J. Fluid Mech.* **783**, 448–473.

Solbakken, S. & Andersson, H. I. 2004 On the drag reduction mechanism in a lubricated turbulent channel flow. *Int. J. Heat and Fluid Flow* **25**, 618–624.

Spalart, P. R., Moser, R. D. & Rogers, M. M. 1991 Spectral methods for the Navier–Stokes equations with one infinite and two periodic directions. *J. Comput. Phys.* **96**, 297–324.

Teo, C. J. & Khoo, B. C. 2009 Analysis of Stokes flow in microchannels with superhydrophobic surfaces containing a periodic array of micro-grooves. *Microfluid Nanofluidics* **7**, 353–382.

Teo, C. J. & Khoo, B. C. 2010 Flow past superhydrophobic surfaces containing longitudinal grooves: effects of interface curvature. *Microfluid Nanofluidics* **9**, 499–511.

Than, P. T., Rosso, F. & Joseph, D. D. 1987 Instability of Poiseuille flow of two immiscible liquids with different viscosities in a channel. *Int. J. Engng Sci.* **25**, 189–204.

Tsai, P. A. 2013 Slippery interfaces for drag reduction. *J. Fluid Mech.* **736**, 1–4.

Tretheway, D. C. & Meinhart, C. D. 2004 A generating mechanism for apparent fluid slip in hydrophobic microchannels. *Phys. Fluids* **16**, 1509.

Türk, S., Daschiel, G., Stroh, A., Hasegawa, Y. & Frohnapfel, B. 2014 Turbulent flow over superhydrophobic surfaces with streamwise grooves. *J. Fluid Mech.* **747**, 186–217.

Vinogradova, O. I. 1999 Slippage of water over hydrophobic surfaces. *Int. J. Miner. Process.* **56**, 31–60.

Watanabe, K., Yanuar & Udagawa, H. 1999 Drag reduction of Newtonian fluid in a circular pipe with a highly water-repellent wall. *J. Fluid Mech.* **381**, 225–238.

Woolford, B., Prince, J., Maynes, D. & Webb, B. W. 2009 Particle image velocimetry characterization of turbulent channel flow with rib patterned superhydrophobic walls. *Phys. Fluids* **21**, 085106.

You, J., Choi, H. & Yoo, J. Y. 2000 A modified fractional step method of keeping a constant mass flow rate in fully developed channel and pipe flows. *KSME Int. J.* **14**, 547–552d.

Ybert, C., Barentine, C., Cottin-Bizonne, Joseph, P. & Bocquet, L. 2007 Achieving large slip with superhydrophobic surfaces: scaling laws for generic geometries. *Phys. Fluids* **19**, 123601.

Zhao, J., Du, X. & Shi, X. 2007 Experimental research on friction-reduction with super-hydrophobic surfaces. *J. Mar. Sci. Appl.* **6**, 58–61.

공기층을 포함한 이상적인 초소수성 표면을 가진 난류채널유동의 직접수치해석

서울대학교 대학원
기계항공공학부
정태용

요약

난류 경계층 유동 내에서 초소수성 표면에 의한 미끄럼 효과는 마찰저항 감소율을 결정하며 이는 초소수성 표면 구조에 영향을 받는다. 본 연구에서는 물-공기 경계면이 편평하다는 가정하에 공기층을 포함한 초소수성 표면을 가진 난류채널유동의 직접수치해석을 수행하였다. 먼저, 표면 요철구조가 없는 이상화된 초소수성 표면을 고려하였다. 공기층 내부의 유동은 전단응력에 의한 유동과 유량이 0인 유동을 고려하였다. 공기층이 두꺼워질수록 미끄럼 길이, 속도, 마찰저항 감소율 모두 증가하였다. 평균 슬립길이는 물 유동의 조건에 상관없이 공기층의 두께에만 영향을 받는다. 또한 본 연구에서는 공기를 직접 계산하여 물-공기 경계면에서 비등방성 미끄럼이 존재한다는 것과 미끄럼 길이의 상대적 크기를 밝혔다. 비등방성 미끄럼을 부가할 수 있는 새로운 미끄럼 모델을 제시하였고, 공기를 같이 풀

었을 때와 마찰저항 감소율이 일치하는 것을 확인하였다. 다음으로, 종방향 홈을 가진 초소수성 표면 주위의 난류 유동을 계산하였다. 이를 통해 마찰저항에 공기분율, 형상길이 뿐만 아니라 공기층의 두께 또한 영향을 미친다는 사실을 밝혔다. 또한 실험에서 사용되는 실제 크기의 초소수성 표면에 대해 연구를 수행하였다. 종방향 홈을 가진 초소수성 표면의 경계면에서도 비등방성 미끄럼이 발생함을 관찰하였다.

주요어: 난류유동, 마찰저항, 물-공기 경계면, 초소수성 표면,
비등방성 미끄럼

학번: 2009-31250